Elsevier Editorial System(tm) for Combustion and Flame
Manuscript Draft

Manuscript Number: CNF-D-12-00451R3

Title: Large-eddy simulation of spray combustion in a gas turbine combustor

Article Type: Accepted Paper

Keywords: Large Eddy Simulation; pdf-methods; stochastic field method; spray

Corresponding Author: Prof. William P Jones, Ph.D.

Corresponding Author's Institution: South Kensington Campus

First Author: William P Jones

Order of Authors: William P Jones; Andrew Marquis; Konstantina Vogiatzaki

Manuscript Region of Origin: UNITED KINGDOM

# Large-eddy simulation of spray combustion in a gas turbine combustor

W. P. Jones, A. J. Marquis, K. Vogiatzaki

*Department of Mechanical Engineering, Imperial College London, Exhibition Road, London SW7 2AZ, UK*

**Abstract**

The paper describes the results of a comprehensive study of turbulent mixing, fuel spray dispersion and evaporation and combustion in a gas-turbine combustor geometry (the DLR Generic Single Sector Combustor) with the aid of Large Eddy Simulations (LES). An Eulerian description of the continuous phase is adopted and is coupled with a Lagrangian formulation of the dispersed phase. The sub-grid scale (*sgs*) probability density function approach in conjunction with the stochastic fields solution method is used to account for *sgs* turbulence-chemistry interactions. Stochastic models are used to represent the influence of *sgs* fluctuations on droplet dispersion and evaporation. Two different test cases are simulated involving reacting and non-reacting conditions. The simulations of the underlying flow field are satisfying in terms of mean statistics and the structure of the flame is captured accurately. Detailed spray simulations are also presented and compared with measurements where the fuel spray model is shown to reproduce the measured SMD and velocity of the droplets accurately.

*Keywords:* Large Eddy Simulation, *pdf*-methods, stochastic field method, spray

*Corresponding Author
*Email address:* w.jones@imperial.ac.uk (W. P. Jones, A. J. Marquis, K. Vogiatzaki )

**Nomenclature**

| Symbol | Description |
|---|---|
| $\mathbf{a}$ | particle acceleration |
| $B$ | Spalding mass transfer number |
| $C_D$ | drag coefficient |
| $C_o$ | model constant ($C_o$ =1) |
| $Cp_\ell$ | liquid specific heat |
| $C_s$ | Smagorinsky parameter |
| $C_V$ | model constant ($C_V$ =1) |
| $dt$ | time interval |
| $d\mathbf{W}_t$ | increment of the Wiener process |
| $F_D$ | drag force |
| $F_g$ | gravitational force |
| $\bar{f}_i$ | momentum exchange between the carrier gas and the dispersed flow |
| $\mathbf{g}$ | gravitational acceleration |
| $h$ | specific enthalpy |
| $h_{fg}$ | latent heat of evaporation |
| $k_{sgs}$ | *sgs* kinetic energy |
| $\dot{m}$ | rate of mass addition to the continuous phase per unit volume through droplet evaporation |
| $m_p$ | particle mass |
| $\dot{\mathcal{N}}$ | rate of change of droplet number through droplet breakup and coalescence |
| $N$ | number of species |
| $N_s$ | number of scalars ($N_s = N + 1$) |
| $p$ | pressure of the gaseous phase |
| $\tilde{P}_{sgs}(\underline{\psi})$ | ensemble of $N$ stochastic fields for each of the $N_s$ scalars |
| $\overline{\mathrm{P}}_{spr}$ | *sgs* spray *pdf* |
| $\dot{\mathcal{R}}$ | rate of change of the droplet radius through evaporation |
| $r$ | droplet radius |
| $Re$ | Reynolds number based on the droplet diameter |
| $Sc_g$ | gas phase Schmidt number at the particle position |
| $Sh$ | Sherwood number |
| $Sh^{(d)}$ | deterministic part of the Sherwood number |
| $Sh^{(st)}$ | stochastic part of the Sherwood number |
| $\widetilde{S}_{ij}$ | filtered rate of strain tensor |
| $\dot{\mathcal{T}}$ | rate of change of droplet temperature caused by heat transfer from the surrounding gas phase |
| $u_j$ | velocity of the gaseous phase |
| $\widetilde{\mathbf{u}}_p$ | filtered gas velocity at the particle position |
| $v$ | droplet velocity |
| $\mathbf{v}_p$ | velocity of the $p^{th}$ particle |

*Greek Symbols*

| | |
|---|---|
| $\Gamma'$ | total - molecular plus *sgs*- diffusion coefficient |
| $\Delta$ | filter width |
| $\eta_i$ | $[-1, 1]$ dichotomic random vector |
| $\theta$ | droplet temperature |
| $\mu_{sgs}$ | *sgs* viscosity |
| $\xi_\alpha^n$ | stochastic fields for $1 \leq n \leq N,\ 1 \leq \alpha \leq N_s$ |
| $\rho$ | density of the gaseous phase |
| $\rho_\ell$ | density of the liquid phase |
| $\rho_p$ | filtered gas density at the particle position |
| $\sigma$ | Schmidt number |
| $\sigma_{ij}$ | viscous stress of the gaseous phase |
| $\tau_{ij}^{sgs}$ | *sgs* stress |
| $\tau_p$ | particle relaxation time |
| $\tau_{sgs}$ | *sgs* mixing time scale |
| $\tau_t$ | sub-grid time scale which determines the rate of interaction between the particle and turbulence dynamics |
| $\phi_\alpha$ | species $\alpha$ |
| $\dot{\omega}_\alpha$ | species $\alpha$ reaction rate |

## 1. Introduction

Numerical simulations complement traditional experimental approaches and can provide a valuable aid to the design of combustion devices with low emissions and more efficient operation. These simulations require accurate models to represent the interaction of turbulence with chemical reactions, and, depending on the complexity of the combustion process additional models for two-phase flows interactions, radiative heat transfer and soot formation may be required. To date practical combustion devices such as gas turbines are mostly designed based on the experimental findings of expensive high quality tests. Simulations of similar geometries could constitute a more economic alternative to experiments but these are rather limited at the present time. The main reason for this is that the computational constraints often lead to simplification such that the simulations are unable to describe all of the complex and interacting physical phenomena taking place over a wide range of length and time scales.

One of the most prominent areas of modern research evolves around liquid fuel combustion. Liquid fuels have a high volumetric and mass energy density and are easy to store and transport. In a practical combustor liquid fuel is atomised into small droplets in order to increase the surface area of fuel exposed to the hot gases and to facilitate rapid vaporisation and mixing with the surrounding air. In addition to this process, in many devices, the spray is injected into a swirling air flow that enhances the mixing between the fuel and the air and thus the evaporation rate. The combustion performance and emissions are mainly influenced by the atomisation of the liquid fuel, the dispersion and evaporation

of the fuel droplets and the mixing of fuel and air. Thus the accurate prediction of the spray dynamics and combustion process is extremely important to determine flame stability over a wide range of operating conditions, to ensure safe and efficient utilisation of energy, and to better understand the mechanisms of pollutant formation.

Reynolds Averaged Simulations (RANS) are currently a major tool for gas turbine combustion chamber designers, but over the last few years Large Eddy Simulation (LES) has undergone considerable development and is starting to make a significant contribution to the design process. In LES a spatial *filter* is applied to the equations of motion. The large energy-containing motions are then computed directly while the effects of the small sub-filter scale motions are modelled. This makes LES an appropriate tool to capture the complicated phenomena including unsteady effects present in a practical combustor.

LES has been applied to the simulation of a wide range of premixed and non-premixed combustion processes demonstrating the ability of the method to migrate from an academic to an industrial tool [1, 2, 3]. Crucial steps in this migration have been the development of numerical algorithms that are flexible enough to handle complex configurations, yet accurate enough to simulate turbulence and its interaction with the physical and chemical processes taking place in a plurality of phases.

In the present work a coupled Eulerian (for the gas-phase flow) and Lagrangian (for the liquid-phase flow) formulation is used to represent the spray dynamics and the interaction between the gas and liquid phases flow [4, 5, 6, 7, 8, 9]. The Eulerian-Lagrangian framework represents a natural approach for flows where a dispersed phase is present. It allows direct modelling of the actual processes that individual droplets undergo (such as break-up, droplet dispersion, wall interactions etc.) in contrast to the more indirect modelling dependence of these processes on the volume fraction of the droplets or their number density distribution required by alternative Euler-Euler approaches. The restriction however of the adopted approach is the need for computationally efficient algorithms especially when the number of droplets is large.

In this paper LES calculations are presented for two operating conditions of a single sector combustor operating at a pressure of 4 bar pressure for which DLR has performed detailed measurements [10, 11]; in particular an isothermal simulation (namely test case E), and a reacting simulation (namely test case A). The focus of the work here is the assessment of the predictive capability of LES with sub-grid scale models for spray dispersion and evaporation and subsequent combustion. The emphasis of the work is placed on the effect of the unresolved velocity and temperature fields on the droplet statistics especially in the region close to the injection point.

## 2. Burner geometry

The configuration under investigation is the DLR Generic Single Sector Combustor (GENRIG): a detailed description can be found in [10, 11]. Velocities and droplet sizes of the evaporating sprays were measured with Phase Doppler

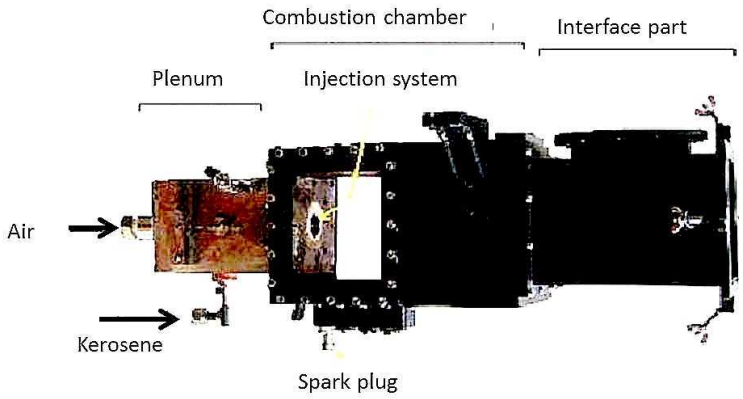


Figure 1: Experimental geometry of the DLR generic combustor [10, 11].

Anemometry (PDA) and temperature was measured with Laser-Induced Fluorescence (OH-LIF). A photograph of the set-up used in the experiments can be seen in Fig. 1. The computational domain used for the CFD calculations consists of two parts: a cylindrical component (80 mm long) that surrounds the two radial air swirlers which are fed by pre-heated air from a plenum, and a rectangular combustor (300 mm long) with a converging duct at the exit as it is shown in Fig. 2. The fuel (commercial aviation kerosene) used for the combusting test is supplied by two opposing fuel lines to an annular fuel gallery, and from there to a vertical slot through a circular array of 36 orifices that surround the base of a prefilmer (see Fig. 3a). The actual pipes, through which the fuel enters, are not included in the computations. Instead the liquid fuel is injected in the form of droplets via an annular ring (represented by 1000 discrete locations [1] from which droplets are injected at random) at an axial location just downstream of the fuel injector prefilmer lip. In addition, the combustor walls have a series of effusion air cooling holes, however as this occurs downstream of the region of interest the effusion cooling air was omitted from the present analysis. A structured, multi-block mesh of the DLR generic combustor was created using ICEM CFD v.11, and consisted in total of 2.2 million cells and 137 blocks ([12]). The mesh is refined at the exit of the swirler and the size of the smallest cells is 0.5 mm (see Figs 2, 3). The size of the largest cells is 5mm and are located in the middle section of the combustor. The simulations were carried out using 16 cores of a Linux cluster comprising Intel Xeon E5404 2.0 GHz CPUs.

[1] It would also have been possible to inject droplets at random locations around the annular ring. However given the uncertainty in spray boundary conditions it is doubtful that this would bring any significant changes

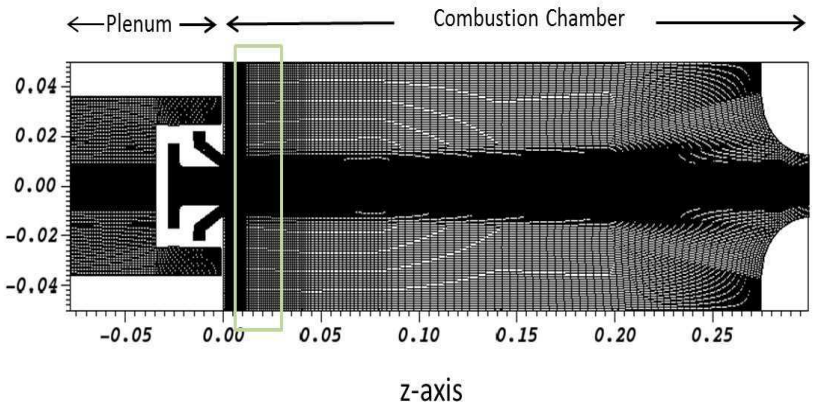


Figure 2: CFD geometry of the DLR generic combustor. The green box indicates the 'window' for which experimental data are available.

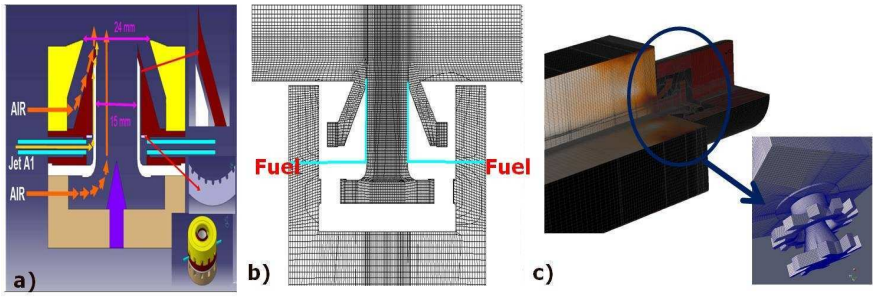


Figure 3: DLR generic combustor grid at the area of the swirler: (a) Schematics of the burner [10, 11]. (b) Slice through injector centre-line showing details of mesh through swirlers. (c) 3-D picture of the double-swirlers

## 3. Numerical details

### *3.1. Mathematical model: Interaction of gaseous and dispersed phase*

In this section the *pdf* approach adopted for the two-phase simulations in the LES context is presented. An Eulerian description of the continuous phase is employed and coupled with a Lagrangian approach for the dispersed phase. The two phases are coupled through the inclusion of the forces exerted on the droplets by the continuous phase and vice-versa and through the rate of phase change. The characteristic dimensions of the dispersed phase are presumed small compared to the length scales of the smallest resolved turbulent motions, enabling the droplets to be viewed as point sources with respect to the continuous phase. Stochastic models are introduced to account for the influence of *sgs* motions on dispersion and evaporation. The effect of particles on turbulence is poorly understood, with most studies being conducted in the context of Reynolds averaged approaches. In the present work the possible modulating effects of *sgs* motions and *sgs* dissipation are ignored. No attempt is made at modelling film breakup and droplet formation and the dispersed phase is also presumed dilute so that collisions, coalescence and agglomeration are ignored [13]. It is recognised that very close to the fuel injector this latter assumption is likely to be violated. In reality, the fuel issues into the combustor in the form of a thin film, which then undergoes breakup to form droplets. We do not attempt to model this breakup process directly but rather instead apply an ansatz of the spray inlet conditions so as to reproduce the measure profiles at z=7mm. The local errors ie those arising in the immediate vicinity of the injection point, associated with this process are greater than those associated with the assumption of a dilute dispersed phase.

In the LES calculations the density-weighted filtered Navier-Stokes equations, with the contribution of the dispersed phase included, can be written as:

$$\frac{\partial \overline{\rho}}{\partial t} + \frac{\partial \overline{\rho}\widetilde{u}_j}{\partial x_j} = \bar{\dot{m}} \tag{1}$$

$$\frac{\partial \overline{\rho}\widetilde{u}_i}{\partial t} + \frac{\partial \overline{\rho}\widetilde{u}_i\widetilde{u}_j}{\partial x_j} = -\frac{\partial \bar{p}}{\partial x_i} + \frac{\partial \bar{\sigma}_{ij}}{\partial x_j} + \frac{\partial \tau_{ij}^{sgs}}{\partial x_j} + \bar{f}_i \tag{2}$$

where $\sigma_{ij}$, $\rho$, $u_j$ and $p$ represent the viscous stress, density, velocity and pressure of the gaseous mixture respectively. The term $\dot{m}$ represents the rate of mass addition to the continuous phase per unit volume through droplet evaporation and $f_i$ is the force per unit volume exerted on the continuous phase by the dispersed phase. The over bars and tildes represent the spatially filtered and density weighted filtered values with a filter width $\Delta$ respectively. The unknown sub-grid stresses are approximated using the Smagorinsky model [14], where the deviatoric part of the sub-grid stress is related to the filtered rate of strain tensor via $\tau_{ij}^{sgs} = \mu_{sgs}\widetilde{S}_{ij}$ with the *sgs* viscosity given by $\mu_{sgs} = \bar{\rho}C_s\Delta^2||\widetilde{S}_{ij}||$; $||\widetilde{S}_{ij}||$ represents the Frobenius norm. The filter width is taken as the cube root of the local grid cell volume. The parameter $C_s$, which is the Smagorinsky parameter, is determined as a function of space and time using the dynamic model of [15].

If, as in the present case for simplicity, variations in thermodynamic pressure are neglected, then the equations describing species mass fractions and enthalpy have a similar form. Hence, the equations for the $N_s$ scalars required to describe combustion can be written:

$$\frac{\partial \overline{\rho}\widetilde{\phi}_\alpha}{\partial t} + \frac{\partial \overline{\rho}\widetilde{\phi}_\alpha \widetilde{u}_j}{\partial x_j} = \frac{\partial}{\partial x_j}\left(\frac{\mu}{\sigma}\frac{\partial \widetilde{\phi}_\alpha}{\partial x_j}\right) + \frac{\partial \overline{J}_j^{sgs}}{\partial x_j} + \overline{\dot{m}}_\alpha(\underline{\phi}) + \overline{\rho\dot{\omega}}_\alpha(\underline{\phi}) \qquad (3)$$

where a Lewis number of one is assumed so that $\sigma$ is the Prandtl or Schmidt number as appropriate. The filtered source term, $\bar{\dot{m}}_\alpha$ represents the rate at which $\phi_\alpha$ is added to the continuous phase per unit volume, through droplet evaporation and depends on the properties of both the dispersed and continuous phases. The former dependence has been dropped in the interests of compactness. The phase exchange source terms are obtained from the volume-averaged contributions of the dispersed phase, eg $\bar{\dot{m}} = \frac{1}{\Delta^3}\sum_{p=1}^{n}\dot{m}_{(p)}$, where the subscript $(p)$ refers to the $p^{th}$ droplet. The presence of the interaction source terms describes two-way coupling between the continuous and the dispersed phases. During the droplet motion, droplet-turbulence interactions occur: the droplets are dispersed by the turbulence of the continuous phase and the turbulence of the continuous phase is modulated by the presence of droplets. The characteristics of these interactions are captured by the momentum exchange between the carrier gas and the dispersed flow through $\bar{f}_i$. However, in the present case the effects of the droplets on the turbulence of the continuous phase is small since the dispersed phase is dilute.

The evaporation of droplets gives rise to sources of mass and $\phi_\alpha$ for the continuous phase, ($\bar{\dot{m}}$ and $\bar{\dot{m}}_\alpha$). When a liquid droplet is released into a high ambient temperature heat transfer occurs. Initially most of the heat transferred to the droplets increases the droplet temperature (heating period). At some point the temperature of the droplet approaches a crucial point (the saturation temperature, which for kerosene is $549K$) the evaporation rate increases to its maximum value.

The chemical source terms appearing in Eq. (3), $\dot{\omega}_\alpha$, are highly non-linear and cannot therefore be evaluated solely in terms of filtered mean quantities. In the present work a statistical description based on the *pdf* approach [16] is adopted and this will be discussed in Section 3.3.

### *3.2. Modelling of droplet dispersion and evaporation*

Following [17, 18] the dispersed phase is described in terms of a set of macroscopic variables: the droplet velocity, $v$, the droplet radius $r$, the droplet temperature $\theta$, and number, $n$. The required joint *pdf* is $\overline{\mathrm{P}}_{spr}$ $(\mathbf{V}, \mathrm{R}, \Theta, \mathrm{N}, \mathbf{x}, t)$, where $(\mathbf{V}, \mathrm{R}, \Theta, \mathrm{N})$ is the 'phase' space for $(\mathbf{v}, \mathrm{r}, \theta, \mathrm{n})$, which can be obtained,

after suitable modelling, from:

$$\frac{\partial \overline{\mathrm{P}}_{spr}}{\partial t} + \nabla_{\mathbf{v}} \cdot \left(\mathbf{a}\overline{\mathrm{P}}_{spr}\right) + \frac{\partial\left(\dot{\mathcal{R}}\overline{\mathrm{P}}_{spr}\right)}{\partial R} + \frac{\partial\left(\dot{\mathcal{T}}\overline{\mathrm{P}}_{spr}\right)}{\partial \Theta} + \frac{\partial\left(\dot{\mathcal{N}}\overline{\mathrm{P}}_{spr}\right)}{\partial N} = 0 \tag{4}$$

where $\mathbf{a}, \dot{\mathcal{R}}$, and $\dot{\mathcal{T}}$ represent the particle acceleration, the rate of change of the droplet radius through evaporation and the rate of change of droplet temperature caused by heat transfer from the surrounding gas phase respectively. Finally $\dot{\mathcal{N}}$ is the rate of change of droplet number through droplet breakup and coalescence. These rates of change terms can be written in the general form:

$$\mathrm{E}\left(\frac{\mathrm{D}\psi_k}{\mathrm{D}t}\middle|\, \mathbf{\Psi} = \mathbf{\Phi}\right) \text{ where } \mathbf{\Phi} = \mathbf{v}, \mathrm{r}, \theta \text{ and } \mathrm{n}$$

which represents the expected value of $\frac{\mathrm{D}\psi_k}{\mathrm{D}t}$ conditioned upon $\mathbf{\Psi} = \mathbf{\Phi}$ anywhere in the filter volume.

Equation (4) is an exact unclosed hyperbolic partial differential equation for the joint *pdf* of the spray in which the filtered conditional Lagrangian rates of change are the cause of the indeterminacy. In order to solve the modelled form of Eq. (4) it is first replaced with an equivalent Ito system, [19], of stochastic differential equations, (*sde's*) describing the trajectories of stochastic particles in the phase space $(\mathbf{V}, \mathrm{R}, \Theta, \mathrm{N})$. These stochastic particles do not necessarily represent individual physical droplets but rather a group of droplets with identical physical properties (size, velocity, temperature). These groups of particles serve to increase the accuracy of the spray statistics and reduce the computational requirements. The particles are inertial particles and follow the Stokes law stating that the drag force $F_D(t)$ exerted by the fluid on the particles is proportional to the difference between the background fluid velocity and the particle velocity and consequently the particle trajectories follow the system of equations:

$$d\mathbf{x}_p = \mathbf{v}_p dt \tag{5}$$

$$m_p \frac{d\mathbf{v}_p}{dt} = F_D + F_g \tag{6}$$

where the subscript $p$ indicates the $p^{th}$ particle (droplet). The term $F_D$ represents the drag force and $F_g$ the gravitational force. Basset forces are ignored since the droplet density (kerosene) is much higher than the ambient density (air).

The motion of a stochastic particle in a turbulent flow field can be viewed as a random process with position determined by a deterministic part, evaluated in terms of filtered values and a stochastic component arising from the *sgs* turbulent motions of the gas phase. In this study only viscous drag and gravitational forces are considered and a stochastic Markov model [17, 20] is used to represent the influence of the unresolved carrier gas velocity fluctuations experienced by a

stochastic particle $p$ over a time interval $dt$ which is added to the deterministic contribution:

$$d\mathbf{v}_p = \tau_p^{-1}\left(\widetilde{\mathbf{U}}_p\left(t\right) - \mathbf{v}_p\right)dt + \frac{\rho_\ell - \bar{\rho}_p}{\rho_\ell}\mathbf{g}dt + \left(C_o\frac{k_{sgs}}{\tau_t}\right)^{1/2}d\mathbf{W}_t \tag{7}$$

where $\rho_\ell$ is the liquid density, $\mathbf{v}_p$ is the velocity of the $p^{th}$ particle, $\bar{\rho}_p$ and $\widetilde{\mathbf{u}}_p$ are the filtered gas density and velocity at the particle position, $k_{sgs}$ is the unresolved kinetic energy of the gas phase, $C_o$ is a model constant assigned the value unity, $d\mathbf{W}_t$ represents the increment of the Wiener process and $\mathbf{g}$ is the gravitational acceleration. Finally, $\tau_t$ is a sub-grid time scale which determines the rate of interaction between the particle and turbulence dynamics, defined as [20]:

$$\tau_t = \tau_p\left(\frac{\tau_p}{\frac{\Delta}{\sqrt{k_{sgs}}}}\right)^{0.6} \tag{8}$$

The particle relaxation time, $\tau_p$ is given by: $\tau_p^{-1} = \frac{3}{8}\frac{\rho_f C_D}{\rho_p R}|\widetilde{\mathbf{u}}_p - \mathbf{v}_p|$, where the drag coefficient $C_D$ is obtained from [21]:

$$C_D = \begin{cases} \frac{24}{Re}\left(1 + \frac{Re^{2/3}}{6}\right) & : \quad 0 < Re < 1000 \\ 0.424 & : \quad Re \geqslant 1000 \end{cases} \tag{9}$$

where $Re$ is the Reynolds number based on the droplet diameter and the relative velocity of the droplet with respect to the gas phase. The *sgs* kinetic energy is obtained using equilibrium arguments from $k_{sgs} = 2\Delta C_s^{2/3}\tilde{S}_{ij}\tilde{S}_{ij}$. If it is assumed that the temperature within each droplet is uniform and that equilibrium conditions prevail at the surface, [22, 23] then the droplet temperature $T_p$ and mass $m_p$ can be obtained from:

$$dm_p = 2\pi r_p\frac{\mu_g}{Sc_g}Sh\ln(1+B)dt \tag{10}$$

$$dT_p = \frac{NuCp_g}{3Pr_gCp_\ell}\frac{(T_g - T_p)}{\tau_p}dt + \frac{h_{fg}}{Cp_\ell}\frac{dm_p}{m_p} \tag{11}$$

where $h_{fg}$ is the latent heat of evaporation, $Cp_\ell$ is the liquid specific heat, $Sc_g$ is the gas phase Schmidt number at the particle position, $Sh$ is the Sherwood number, $Nu$ is the Nusselt number, and $B$ is the Spalding mass transfer number,. The time scale $\tau_p$ is defined as before.

In the current approach the droplets are considered to have sizes smaller than the filter size and thus their trajectories are affected by both large (resolved) and small (unresolved) scales. If equations (7), (10) and (11) are evaluated in terms of the filtered quantities only, the direct effects of sub-grid velocity fluctuations (small scales) would not be included. The relative velocity between the droplets and the flow and the gas-phase temperature and vapour mass fraction are filtered versions of the complete instantaneous fields. It would only be possible for the

droplets to 'feel' the (indirect) effect of the sub-grid scales through the sub-grid models that are used for the closure of the filtered momentum and continuity equations. In order to account for the direct effects of small scales on the droplets the stochastic model of [18] is adopted in the present work. This is substantially different from that of other studies of spray combustion (see for example [7, 24])

The parameter governing convection, $Sh$, is rewritten as the sum of the resolved deterministic contribution and a random part ($Sh = Sh^{(d)} + Sh^{(st)}$). The deterministic contribution is obtained in a conventional manner from the correlations given in [25, 26]. The term $Sh^{(st)}$ accounts for the missing *sgs* turbulence effects, which should vanish as LES approaches DNS and be consistent with the Ranz-Marshall correlation (*ie* capture in a similar fashion unresolved effects). Thus the stochastic contribution to Eq. (10) is represented by:

$$Sh^{(st)}dt = C_V Sc_g^{1/3} \sqrt{\frac{\rho_g k_{sgs}^{1/2} 2r_p |dW^t|}{\mu_g}} \tau_p^{3/4} \tag{12}$$

where $C_V$ is a model constant assigned a value of unity [18]. The properties of the gaseous phase are evaluated using the one-third rule [27, 28, 29].

It is important to note that $k_{sgs}$ (used in both (Eqs. (7) and (12)) is modelled proportional to the *sgs* viscosity. A dynamic model is used to determine $C_s$ and a zero value of this implies no sub-grid fluctuations. As a consequence in areas of the flow that are well resolved the *sgs* turbulence kinetic energy will tend to zero. The model is thus consistent with the findings of Pozorski et al. [30] who performed a systematic study of the direct effect of sub-grid scale velocity fluctuations on particle motion in forced isotropic turbulence. It was shown that in poorly resolved regions, where the *sgs* kinetic energy was more than 30% of the total the effect on droplet motion was more pronounced. However, in well resolved areas, where the amount of energy in the sub-grid scales was small its effect was not strong.

The spray model, equations (4)-(12) has previously been applied to the simulation of dispersion in a water droplet laden mixing layer, [17, 31], to evaporating acetone and kerosene sprays, [18, 32] and to an axisymmetric combustion chamber, [33, 34].

### *3.3. Combustion model*

For the low-Mach number gaseous phase, multicomponent reacting mixture, the scalars of interest are the $N_s$ scalar quantities which include the $N$ species mass fraction and the mixture specific enthalpy $h$ governed by Eq. (3) ($N_s = N + 1$). An evolution equation for the one-point, one-time *pdf* for the set of $N_s$ variables that determine the local thermo-chemical state of a reacting system can then be derived using established techniques, [16, 35, 36]. The main advantage of the *pdf* approach is that the chemical and phase exchange source terms of the transport equations for the scalar quantities, appear in a closed form, whereas the molecular transport or micro-mixing must be modelled. Using the filtering

operation and following Gao et al. [37] the equation describing the evolution of the density weighted sub-grid (or more strictly the density weighted filtered fine grained) *pdf* for the $N_s$ scalars can be derived:

$$\frac{\partial \overline{\rho}\widetilde{P}_{sgs}(\underline{\psi})}{\partial t} + \frac{\partial \overline{\rho}\tilde{u}_j\widetilde{P}_{sgs}(\underline{\psi})}{\partial x_j} - \frac{\overline{\rho}\dot{m}(\underline{\psi})}{\rho(\underline{\psi})}\widetilde{P}_{sgs}(\underline{\psi}) + \sum_{\alpha=1}^{N_s}\frac{\partial}{\partial\psi_\alpha}\left[\overline{\rho}\dot{\omega}_\alpha(\underline{\psi})\widetilde{P}_{sgs}(\underline{\psi})\right] + \sum_{\alpha=1}^{N_s}\frac{\partial}{\partial\psi_\alpha}\left[\frac{\overline{\rho}\left(\dot{m}_\alpha(\underline{\psi}) - \dot{m}(\underline{\psi})\psi_\alpha\right)}{\rho(\underline{\psi})}\widetilde{P}_{sgs}(\underline{\psi})\right] = -\frac{\partial}{\partial x_i}\left[\left(\overline{\rho u_i} - \overline{\rho}\tilde{u}_i|\,\underline{\phi} = \underline{\psi}\right)\widetilde{P}_{sgs}(\underline{\psi})\right] - \sum_{\alpha=1}^{N_s}\sum_{\beta=1}^{N_s}\frac{\partial^2}{\partial\psi_\alpha\partial\psi_\beta}\left[\left(\frac{\mu}{\sigma}\overline{\frac{\partial\phi_\alpha}{\partial x_i}\frac{\partial\phi_\beta}{\partial x_i}\middle|\,\underline{\phi} = \underline{\psi}}\right)\widetilde{P}_{sgs}(\underline{\psi})\right] \quad (13)$$

All of the terms on the left hand side of Eq. (13) appear in closed form and no modelling is required. In contrast the two terms on the right hand side of Eq. (13) describe the sub-grid transport and micro-mixing. These terms describe processes occurring at the small scales that are not resolved by the LES approach and are therefore unknown and need to be modelled. In the present work the dynamic Smagorinsky sub-grid viscosity model is used for transport and the Linear Mean Square estimation closure (LMSE) [38] is applied for micro-mixing. The model was also proposed independently in stirred reactor studies where it is known as Interaction by Exchange with the Mean (IEM) [39]. The LMSE/IEM mixing model has been widely used in many *sgs-pdf* studies. Including these models, Eq. (13) finally becomes:

$$\frac{\partial \overline{\rho}\widetilde{P}_{sgs}(\underline{\psi})}{\partial t} + \frac{\partial \overline{\rho}\tilde{u}_j\widetilde{P}_{sgs}(\underline{\psi})}{\partial x_j} - \frac{\overline{\rho}\dot{m}(\underline{\psi})}{\rho(\underline{\psi})}\widetilde{P}_{sgs}(\underline{\psi}) + \sum_{\alpha=1}^{N_s}\frac{\partial}{\partial\psi_\alpha}\left[\overline{\rho}\dot{\omega}_\alpha(\underline{\psi})\widetilde{P}_{sgs}(\underline{\psi})\right] + \sum_{\alpha=1}^{N_s}\frac{\partial}{\partial\psi_\alpha}\left[\frac{\overline{\rho}\left(\dot{m}_\alpha(\underline{\psi}) - \dot{m}(\underline{\psi})\psi_\alpha\right)}{\rho(\underline{\psi})}\widetilde{P}_{sgs}(\underline{\psi})\right] = \frac{\partial}{\partial x_i}\left[\left(\frac{\mu}{\sigma} + \frac{\mu_{sgs}}{\sigma_{sgs}}\right)\frac{\partial\widetilde{P}_{sgs}(\underline{\psi})}{\partial x_i}\right] - \frac{\overline{\rho}}{\tau_{sgs}}\sum_{\alpha=1}^{N}\frac{\partial}{\partial\psi_\alpha}\left[(\psi_\alpha - \phi_\alpha(\mathbf{x},t))\tilde{P}_{sgs}(\underline{\psi})\right] \quad (14)$$

where $\sigma_{sgs}$ has been assigned a value of 1.0 and $\dot{\omega}_\alpha(\underline{\psi})$ is the net species formation rate through chemical reaction. Following, eg [40, 41] the sub-grid mixing time scale is assumed given by:

$$\tau_{sgs}^{-1} = C_d\frac{\mu + \mu_{sgs}}{\bar{\rho}\Delta^2} \quad (15)$$

This has the property that $\tau_{sgs}$ tends to zero as the filter width, $\Delta$ tends to zero, which correctly drives the *pdf* towards a $\delta$-function as this limit is approached.

The high dimensionality of equation (14) does not allow a solution by conventional difference schemes because the cost increases exponentially as the number

of scalars is increases. The approach commonly used is that based on the use of Lagrangian stochastic particles where an ensemble of particles is used to represent the joint *pdf* [16, 38, 42]. In the current work an alternative approach is followed. Equation (14) is solved using the Eulerian stochastic field method. The $\widetilde{P}_{sgs}(\underline{\psi})$ is represented by an ensemble of $N$ stochastic fields for each of the $N_s$ scalars, namely $\xi^n_\alpha(\mathbf{x},t)$ for $1 \leq n \leq N,\ 1 \leq \alpha \leq N_s$, viz:

$$\widetilde{P}_{sgs}(\boldsymbol{\psi};\mathbf{x},t) = \frac{1}{N}\sum_{m=1}^{N}\int_\Omega \rho G(\mathbf{x}-\mathbf{x}';\Delta(\mathbf{x}))d\mathbf{x}' \times \prod_{\alpha=1}^{N_s}\delta\left[\psi_\alpha - \xi^m_\alpha(\mathbf{x},t)\right] \quad (16)$$

Two formulations of the method can be devised depending on whether an Ito or Stratonovich interpretation of the stochastic integral is adopted; for a description of these alternatives see [43] and [44]. In the present work the Ito formulation is adopted in which case the stochastic fields are continuous and differentiable in space and continuous though not differentiable in time. The method has been successfully applied in various problems in the context of RANS [45, 46] as well as LES [33, 34, 40, 41]. In the present study the influence of the *sgs* fluctuations of the dispersed phase is neglected and the stochastic fields evolve according to:

$$\begin{aligned}
\bar{\rho}\mathrm{d}\xi^n_\alpha = \quad & - \quad \bar{\rho}\tilde{u}_i\frac{\partial\xi^n_\alpha}{\partial x_i}\mathrm{d}t + \frac{\partial}{\partial x_i}\left[\Gamma'\frac{\partial\xi^n_\alpha}{\partial x_i}\right]\mathrm{d}t + \bar{\rho}\sqrt{\frac{2\Gamma'}{\bar{\rho}}}\frac{\partial\xi^n_\alpha}{\partial x_j}\mathrm{d}W^n_i \\
& - \quad \frac{\bar{\rho}}{2\tau_{sgs}}\left(\xi^n_\alpha - \widetilde{\phi}_\alpha\right)\mathrm{d}t + \bar{\rho}\dot{\omega}^n_\alpha(\underline{\xi}^n)\mathrm{d}t \\
& + \quad \left(\dot{m}_\alpha(\widetilde{\phi}_\alpha) - \dot{m}(\widetilde{\phi}_\alpha)\xi^n_\alpha\right)\mathrm{d}t
\end{aligned} \quad (17)$$

where $\Gamma'$ represents the total - molecular plus sub-grid scale - diffusion coefficient and $dW^n_i$ represents increments of a vector Wiener process, different for each field but independent of the spatial location $\mathbf{x}$. The above equation preserves the boundedness of the scalar as the gradient of the field vanishes when the scalars go to extrema and therefore the stochastic contribution tends to zero. Each field satisfies the mass conservation and boundedness properties of the modelled *pdf* equation: the species mass fraction will remain positive and sum to unity. It is important to stress that the stochastic fields given by Eq. (17) do not represent any particular realisation of the real field, but rather form an equivalent stochastic system (both sets have the same one-point *pdf*) that is smooth on the scale of the filter width. All one point moments can be obtained from averaging over the stochastic fields, eg.:

$$\widetilde{\phi}_\alpha = \frac{1}{N}\sum_{1}^{N}\xi^n_\alpha \quad (18)$$

*3.3.1. Chemical Scheme*

A detailed description of kerosene combustion involves a very large number of chemical species and reaction steps. From a computational standpoint an

essential aspect of combustion modelling using the *pdf* methodology (and most others approaches) is a reduction in the number species for which transport equations have to be solved to manageable proportions. For this reason a global mechanism for kerosene combustion has been devised, based on the reduced mechanism of [47] for the combustion of alkanes. Kerosene is represented by $C_{12}H_{23}$ and reaction involves the following four global reaction steps:

$$\begin{array}{rcll} C_{12}H_{23} + 6O_2 & \rightharpoonup & 12CO + 11.5H_2 & (i) \\ C_{12}H_{23} + 12H_2O & \rightharpoonup & 12CO + 23.5H_2 & (ii) \\ H_2 + \frac{1}{2}O_2 & \rightleftharpoons & H_2O & (iii) \\ CO + H_2O & \rightleftharpoons & CO_2 + H_2 & (iv) \end{array}$$

with rate constants[2]:

$$\begin{aligned} \dot{r}_i &= 4.4 \times 10^{11} \exp\left(\frac{-30000}{\mathcal{R}T}\right) \rho^{0.75} \sqrt{n}_{C_{12}H_{23}} {n_{O_2}}^{1.25} \\ \dot{r}_{ii} &= 3.00 \times 10^{8} \exp\left(\frac{-30000}{\mathcal{R}T}\right) \rho\, n_{C_{12}H_{23}}\, n_{H2O} \\ \dot{r}_{iii} &= \frac{2.50 \times 10^{16}}{T} \exp\left(\frac{-40000}{\mathcal{R}T}\right) \rho^{0.75} \sqrt{n}_{H_2} {n_{O_2}}^{2.25} / n_{H2O} \\ \dot{r}_{iv} &= 2.75 \times 10^{9} \exp\left(\frac{-20000}{\mathcal{R}T}\right) \rho\, n_{CO}\, n_{H2O}) \end{aligned}$$

The performance of the scheme in laminar premixed flames is discussed in [48]. In the present context it is to be noted that for a stoichiometric kerosene-air mixture at a pressure of 4bar and an initial temperature of 550K the mechanism predicts a burning velocity of around 145cm/s compared with a value of 170cm/s given by the detailed skeletal mechanism [49, 50]. Although the value of 145cm/s is probably a little on the low side the few measurements of kerosene-air flame speed available are insufficient to justify change.

## 4. Simulation specifics

The in-house block-structured, parallel, boundary conforming coordinate LES code, BOFFIN-LES, [51] has been used for the calculations presented in this paper. LES was performed for two of the operating conditions at which DLR-AT carried out measurements (see Table 1): an isothermal simulation at condition E, and reacting simulations at condition A. A summary of the mass flow boundary conditions used in these CFD simulations is given in Table 2.

The LES code is based on a finite-volume approach using an implicit low-Mach number formulation with a two-step approximate factorisation pressure correction technique used to ensure mass conservation. Spatial derivatives are approximated with second-order central differences and a Crank-Nicolson

[2]The units of the reaction rates are: $\frac{kg\ mol}{kg\ s}$.

| Oper. Cond. | Inlet Air Pressure | Preheated Air Temperature | Burner AFR |
|---|---|---|---|
| A | 4 bar | 550 K | 20 |
| E | 4 bar | 295 K | - |

Table 1: Operating conditions for the simulated cases

| Operating Conditions | Burner Feed Air M.F.R. | Film Cooling Air M.F.R. | Fuel M.F.R. |
|---|---|---|---|
| A | 59.5 g/s | 17.0 g/s | 2.98 g/s |
| E | 81.3 g/s | 23.2 g/s | - |

Table 2: Mass flow boundary conditions for the simulated cases

scheme is used for temporal discretisation. The convective part of the Ito equations of the stochastic field equations is discretised with a Total Variation Diminish (TVD)-scheme, [52], applied in a linearised implicit manner. The simulations are performed with a filter width equal to the cube root of the local grid cell volume and a dynamic version of the Smagorinsky model is used for the *sgs* stresses. Wall-functions, based on the semi-logarithm law of the wall [53] are applied at all solid boundaries. In combustion chamber flows of the type considered the turbulence in the immediate vicinity of a solid surface and, indeed, the wall shear stress exert a negligible influence on the overall flow structure. Non-reflecting conditions are applied at the outflow boundary. Further details of method can be found in eg [48].

The Weiner process of Eq. (17) is represented by time step increments $\eta_i\sqrt{\Delta t}$ where $\eta_i$ is a $[-1,1]$ dichotomic random vector [19, 54]. Random numbers $\eta^{2i-1}$ for $1 \leq i \leq N/2$ are selected from a dichotomic distribution and the remaining numbers are determined from $\eta^{2i} = -\eta^{2i-1}$ for $1 \leq i \leq N/2$. Providing an even number, N of fields is selected the procedure ensures that the mean and variances of the random vector are zero and unity regardless of the number of fields. The Ito process is discretised using the Euler-Maruyama scheme [54], which is a variant of the commonly used Euler scheme. For the particle transport equation similar schemes are used. The Euler-Maruyama scheme is used for discretisation and the increment of the Weiner process, $\Delta W$ is represented by $\xi_i\sqrt{\Delta t}$ where $\xi_i$ is a random vector sampled from a standard Gaussian distribution, independent for each time step and each coordinate.

For the non-reactive case a time-step of 0.2 $\mu s$ was chosen. The geometry under consideration is 0.38m long and given an average bulk velocity of 40m/s one flow-through time corresponds to 0.0095 sec. Thus initially 60,000 time-steps, corresponding to around 1.3 flow-through times, were performed in order to flush-out the initial conditions and allow the flow field to develop. Statistics were then gathered just over a further 4.2 flow-through times, 210,000 time-steps. The inlet velocity for the reactive case is higher (around 60m/s) which results in mean flow through time of 0.0063s. For the reactive case 120,000 time steps (0.012s) for the corresponding isothermal case without the spray was

run initially to allow the underlying flow field to develop, followed by another 180,000 time steps with injection of spray and reaction (0.018sec) to 'wash out' the initial conditions. Statistics were then collected over a further 300,000 time steps (0.03sec).

Reacting simulations were performed at operating condition A using the coupled Eulerian (continuous phase) and Lagrangian (liquid phase) formulation that was described in the previous section. The fuel used is a commercial aviation kerosene (Jet-A) and is represented as $C_{12}H_{23}$ with properties given by Rachner, [55]. The combustion process is described by a global 4-step, 7-species reaction mechanism [47]. The liquid fuel flow is modelled using particles that are injected in a ring of discrete locations at an axial location just downstream of the fuel injector prefilmer lip. A range of particle size groups are injected, using a Rosin-Rammler *pdf*. The droplet temperature is 295 K and the injection velocity is 50 m/s, a value estimated from the measurements available at 7mm downstream of the injection ring. A trial and error procedure was used to determine the injection angle. An initial estimate of injection angle was obtained by geometrical considerations, see Fig. 4, and a series of computations were then run for the range of angles 120°-170°. A value of 160°was found to result in good agreement with the measured profile at 7mm downstream. The droplets are presumed to 'bounce' on impact with a solid surface, although very few droplets do so in the present study. The time-step used was 0.1 $\mu s$ and after the start-up a number close to one million droplets were present in the domain at each time step. The algorithm for the combined Eulerian-Lagrangian model is as follows:

- The equations for the continuous phase are first solved to determine the gas-phase properties everywhere in the domain.
- The gas-phase properties are interpolated from the Eulerian grid to the particle position using a trilinear interpolation scheme.
- The particle properties are updated by integrating the stochastic differential equations in time.
- Statistical averages are calculated for the dispersed phase using an ensemble average from the set of the particles found in the appropriate Eulerian cell.
- The source terms of the flow field equations due to the dispersed phase are updated; to be used by the continuous-phase solver.
- The process is repeated.

## 5. Results and discussion

### *5.1. Isothermal Simulations: Case E*

Attention is first directed towards an evaluation of the ability of the LES formulation to reproduce the velocity field characteristics of the continuous gas

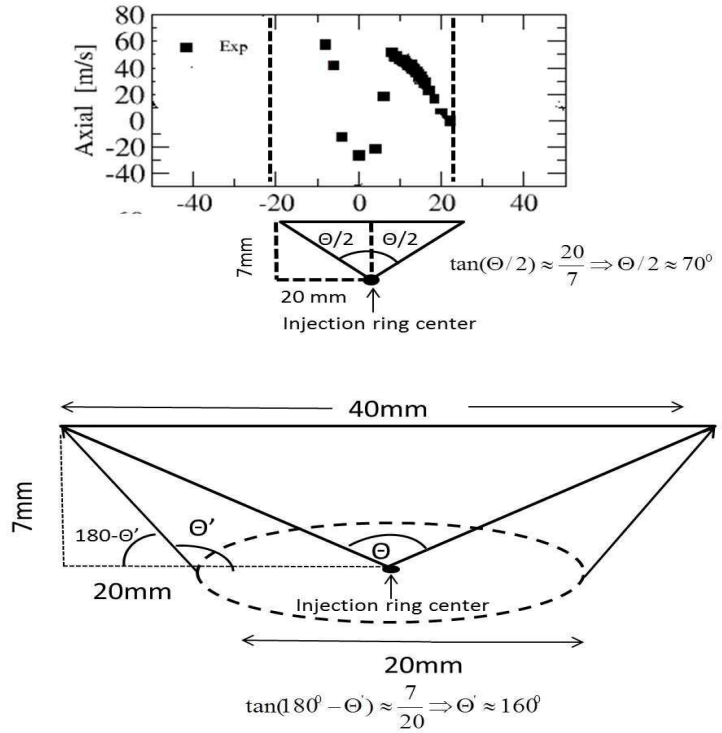


Figure 4: Schematic of the geometrical approach in order to define the injection angles Θ, Θ′. The plot on the top of the figure demonstrates the experimental data of mean droplet velocity at z=7mm

phase. Air at temperature of 295 K is injected into the plenum and acquires a swirling motion as it passes through the vanes of the double swirler. Figures 5 and 6 show a comparison of the measured, [10, 11] and simulated time averaged and *rms* profiles of the axial, radial and azimuthal velocity components at planes normal to the combustor axis at two locations (5 mm and 10 mm) downstream of the fuel injector. As is evident the simulations of both mean and *rms* of the three velocity components compare well with the measured data. The size of the recirculation zone and the magnitude of all three components is accurately reproduced. It can be observed that the mean velocity downstream of the injector is closely axisymmetric whilst the *rms* profiles indicate a significant amount of unsteadiness. The simulations show some asymmetry for z=10mm which however can be explained form the rather short time of the simulation due to computational restrictions.

### *5.2. Reactive Simulations: Case A*

The reacting flow simulations were started by first simulating a non-reacting flow with liquid kerosene injected from the injection ring. The evolution of the injection process is illustrated in Fig. 7. The fuel mass flow is set to 2.98 g/sec

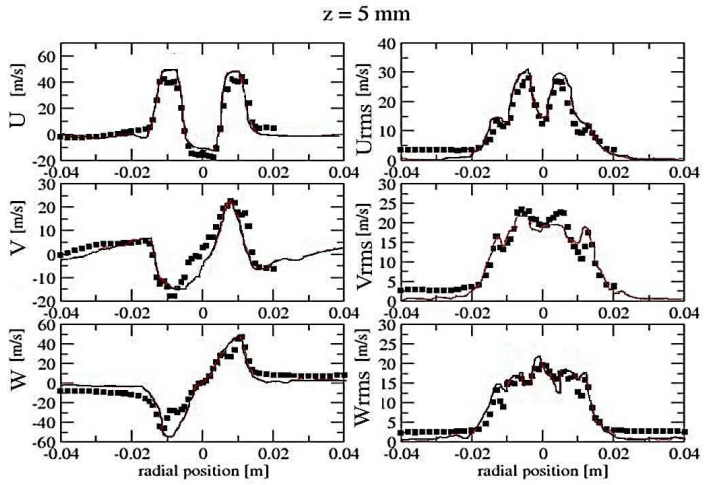


Figure 5: Radial profiles of axial, radial and tangential mean (left) and *rms* (right) of velocity at z = 5mm for isothermal flow field. Squares represent the experiments [10, 11] and solid lines the LES simulations.

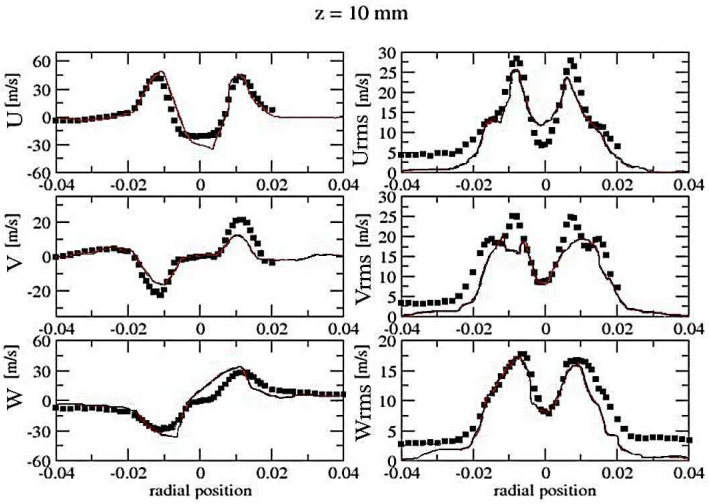


Figure 6: Radial profiles of axial, radial and tangential mean (left) and rms (right) of velocity at z = 10mm for isothermal flow field. Squares represent the experiments [10, 11] and solid lines the LES simulations.

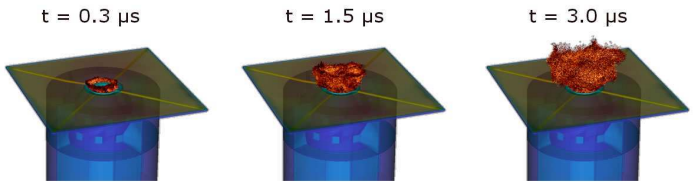


Figure 7: Snapshots of the spray injection at three times.

corresponding to an AFR of 20. Once spray particles are injected into the chamber and, as the air injected in the inlet is already preheated (550 K), the droplets start evaporating creating a combustible mixture. The air-fuel mixture is ignited using an essentially unstrained 'mixed is burnt' flamelet model in place of the sgs-*pdf* model. A snapshot of temperature arising from the flamelet simulations can be seen in Fig. 8a.

The burning flamelet solution was then used to initiate the *sgs-pdf* equation/stochastic fields method. Figure 8b shows a snapshot of the temperature field arising with this method. The solutions with the two models are quite different. It is evident that the areas of the highest temperatures ($> 2100$ K) are more localised with the flamelet whereas the temperature is more uniformly distributed with the *sgs-pdf* method. This provides an indication of the importance of the combustion model in the simulation of the instantaneous (and consequently the mean) flame structure. In the following sections the influence of the *sgs-pdf* model on the simulations of the flow field and how this affects the spray statistics is investigated. Following [40] eight stochastic fields have been used to characterise the influence of the sub-grid fluctuations; in [40] eight and sixteen fields were found to give very similar results. The influence of the number of stochastic fields has also been investigated in [56] where similar conclusions are drawn. Results were also obtained using a single field; a special case where the effects of sub-grid fluctuations on combustion are neglected and the *sgs-pdf* collapses to delta functions at the filtered values of the scalars.

Figure 9 shows contour plots of the mean axial velocity of the non-reactive case E (Fig. 9a) and the reactive case A (Fig. 9d). For a more detailed analysis two extra computations, not corresponding to any measured case, have been included. Figure 9b shows results for the same input velocity and temperature as the reactive case A without the liquid fuel spray and thus no combustion occurs. Figure 9c corresponds to the same conditions but with the spray included; no external ignition process is applied and thus no combustion occurs. It is evident in all four cases the mean axial velocity field displays a symmetrical cone-angle as it exits the fuel injector together with a strong recirculation zone (area coloured in blue) in the centre of the cone. For the reactive test case A the recirculation zone is stronger and extends further downstream compared to the other three cases which is consistent with the lower densities arising due to combustion. In addition, it can be seen that the presence of droplets does not change the flow

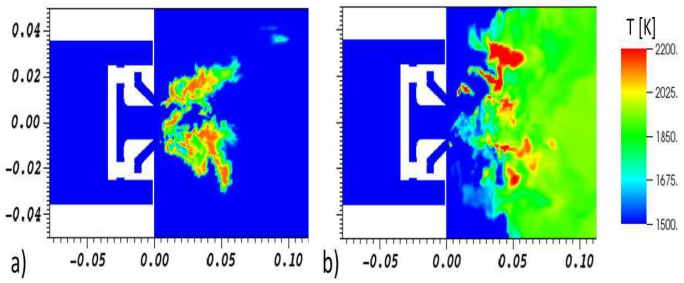


Figure 8: (a) Snapshot of temperature from the flamelet simulation after 0.006s. (b) Snapshot of temperature from the *pdf* simulation after 0.042s

field significantly, (Fig. 9b and Fig. 9c), the spray is dilute and thus the forces exerted on the continuous phase by the droplets, term $\overline{f}_i$ of Eq. (2), are small.

Figure 10 compares a picture of the DLR-AT measured temperature just downstream of the fuel injector [10, 11] with LES simulations using one and eight stochastic fields. The experimental temperatures were calculated from absolute OH densities which were in turn measured using simultaneous PLIF and absorption. In lean flames and under the assumption of OH being in chemical equilibrium, temperatures can be inferred from OH concentrations. There is some uncertainty at the determination of local OH concentration (less than 30%) mainly because of the uncertainty of the fluorescence quantum yield for the unknown local gas composition. The OH super-equilibrium concentration within the flame front leads to an overestimation of the temperature of about 100K but the relaxation has been reported to take place within less than 50 $\mu$s at 10 bar [10, 11]. As can be seen the V-shape of the flame is captured reasonably well by the simulations. The temperature field for both simulations seems to be somewhat high in the vicinity of the centerline. The distinct 'lobes' of high temperature in the experiment are also reproduced although the lift off height is not accurately reproduced as the lobes from the simulations appear to be located further upstream than is measured. A stable pocket of hot gases in the recirculation zone located around the centerline close to the injection point is also reproduced similar to the experiments. It appears that qualitatively the inclusion of the *sgs* combustion model (by increasing the number of fields from one to eight) does not influence the structure of the flame appreciably. However a more detailed analysis, to follow, involving a comparison of the radial profiles reveals otherwise.

Figs 11 and 12 shows 'slices' of the instantaneous temperature, the instantaneous velocities and droplet diameter at downstream locations that correspond to three positions in the area indicated in Fig. 10. Figure 11 corresponds to the results with eight fields whilst Fig. 12 are those for one field. It can be seen that the higher areas of temperature are located in the outer part of the recirculation

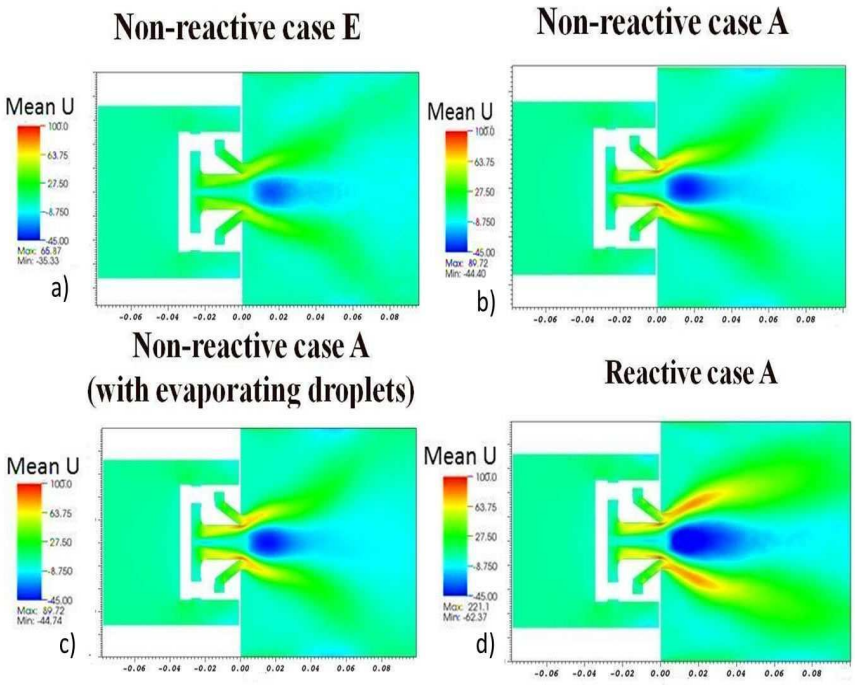


Figure 9: (a) Mean axial velocity for the non-reactive case E. (b) Mean axial velocity for reactive case A without ignition. (c) as (b) but with droplet injection. (d) Mean axial velocity for the reactive case A.

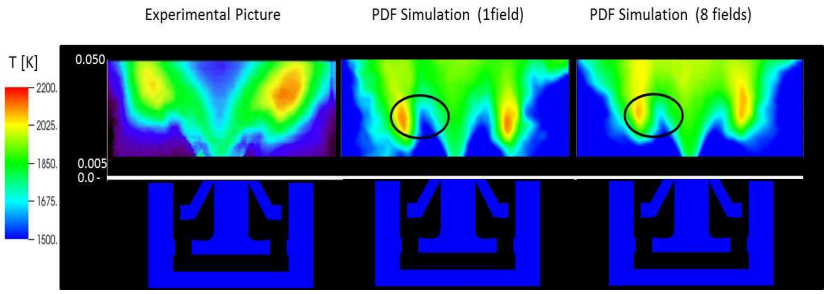


Figure 10: Comparison of OH-PLIF measured mean temperature field (left) with LES with the *pdf* combustion model with one (middle) and eight (right) fields. The white line indicates the swirler exit plane.

bubble. Inside the recirculation bubble the temperatures are high especially at the most downstream location. The instantaneous structure of the flame does not seem to change significantly when the number of fields is increased from one to eight except possibly at $z = 0.045$ where the recirculation zone appears less strong when eight fields are used. Also the temperature distribution is wider at this location.

Figures 13 to 16 show the simulated radial profiles of mean and rms of temperature and axial and radial velocity at different axial locations arising from one field and eight stochastic fields. The first three axial locations correspond to the area close to the injector just before the flow enters the combustion zone (in Fig. 10 the area below the 'lobes') and the other three correspond to axial locations inside the reaction zone, as is indicated by the magnitude and shape of mean temperature profiles.

The profiles of the mean and rms velocities do not change as the number of fields is increased from one to eight, however some small differences (that, as will be demonstrated below, are important when the spray statistics are considered) are evident in the mean and rms temperatures. The increase in the number of fields from one to eight implies that instead of the delta function corresponding to the single field a 'broader' shaped *pdf* is expected to arise with eight fields. With eight stochastic fields the number of samples is equal to the number of fields multiplied by the number of time steps thus allowing the *pdf* to be computed much more accurately. This broadening of the *pdf* is manifested in the radial profiles of temperature as smaller gradients in the region around a radial position of roughly 20mm and in a smaller penetration of the flow into the combustion region (in the black circle of Fig. 10).

Attention is now turned to an investigation of the spray statistics and how these are affected by the combusting flow field. Figures 17 to 19 provide a general overview of the gaseous and liquid phases. More specifically, Fig. 17 shows a 3-D snapshot of the flow field and droplets present (black dots) with the red line representing gas temperatures greater than 1500K while Fig. 18 is a slice through the computational domain with the two coloured V-shaped

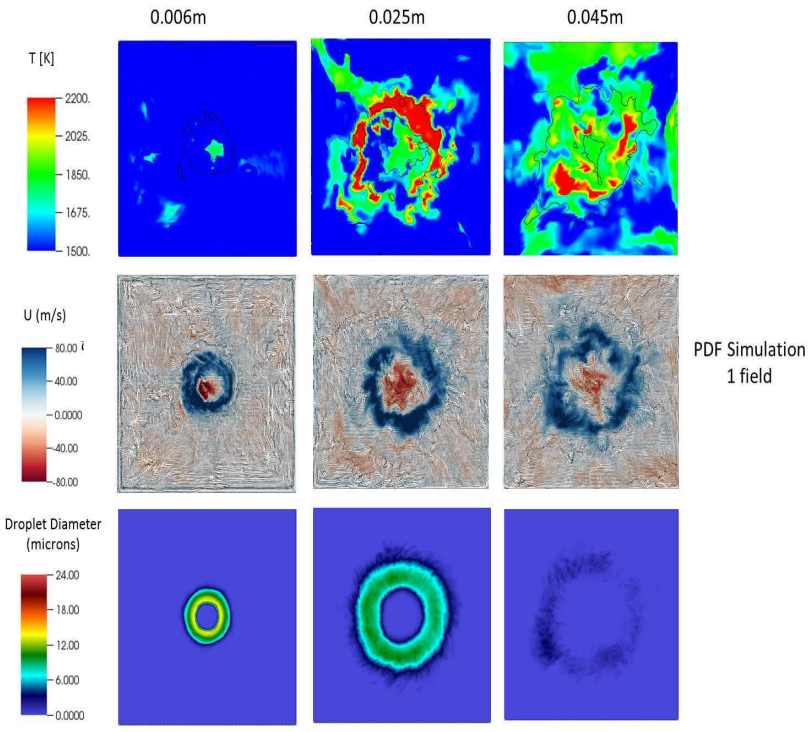


Figure 11: Slices at different axial locations of instantaneous contours for LES calculations with 1 field. Figures at the top show instantaneous temperature fields. Black lines demonstrate the stoichiometric mixture fraction. Figures in the middle show instantaneous velocity field and figures at the bottom the droplet distribution coloured according to their size.

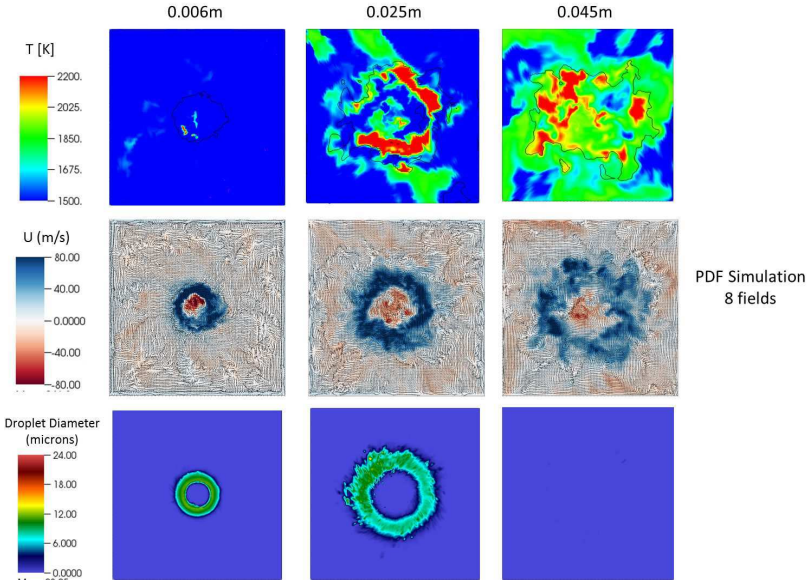


Figure 12: Slices at different axial locations of instantaneous contours for LES calculations with 1 field. Figures at the top show instantaneous temperature fields. Black lines demonstrate the stoichiometric mixture fraction. Figures in the middle show instantaneous velocity field and figures at the bottom the droplet distribution coloured according to their size.

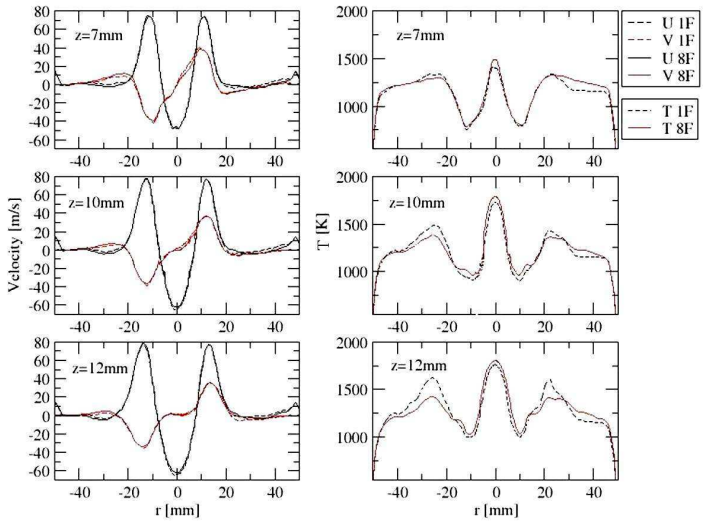


Figure 13: Radial profiles of mean axial and radial velocity (left) and temperature (right) at different axial locations for the reactive case A with LES. Dashed lines represent 1 field predictions and solid lines 8 fields.

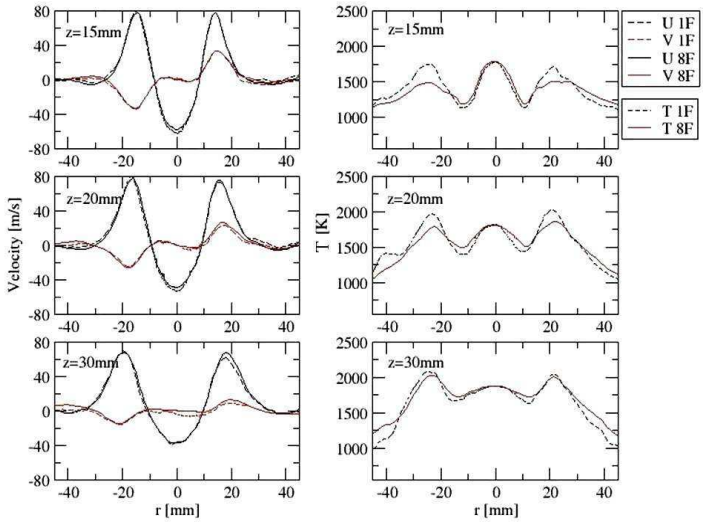


Figure 14: Radial profiles of mean axial and radial velocity (left) and temperature (right) at different axial locations for the reactive case A with LES. Dashed lines represent 1 field predictions and solid lines 8 fields.

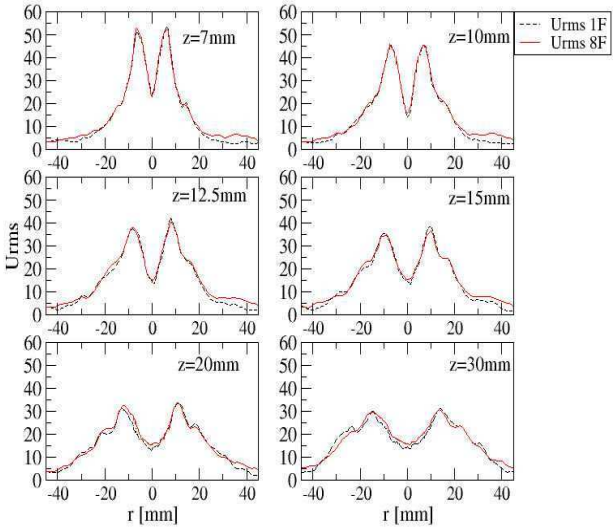


Figure 15: Radial profiles axial velocity rms at different axial locations for the reactive case A with LES. Dashed lines represent 1 field predictions and solid lines 8 fields.

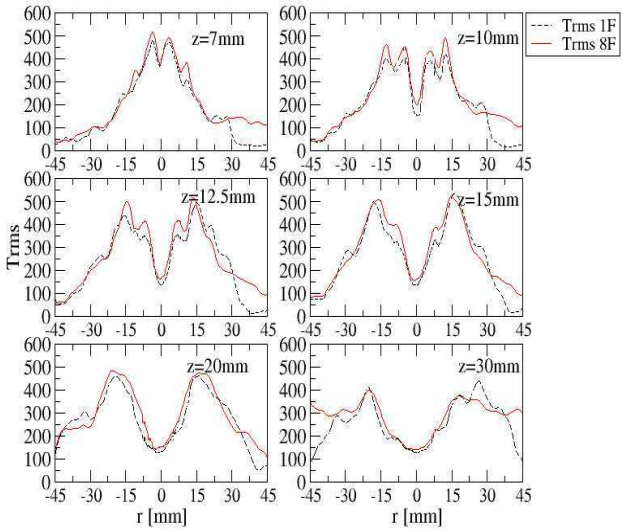


Figure 16: Radial profiles temperature rms at different axial locations for the reactive case A with LES. Dashed lines represent 1 field predictions and solid lines 8 fields.

branches indicating the position of the droplets A vector representation has been used in Fig. 17 to represent the continuous phase flow field.

In Fig. 18 where a slice of the combustor and droplet diameter contours are shown, along with the stagnation contour for the velocity, two recirculation zones are evident. The first recirculation zone arises from the presence of the double swirler and is of particular interest because it is located in between the 'V-shaped' spray stream and is expected to affect the mixing of the fuel vapour with the preheated air. The second recirculation zone is located close to the combustor wall on the sides of the lobes and is expected to stabilise the opening angle of the spray. Unfortunately, experimental measurements of the mean and rms of the gas phase velocity components are not available in order to assess the accuracy of the LES simulations. However, given that the grid is fine enough to reproduce accurately the non-reactive test case E (see Figs 5 and 6) and that the flame structure is well reproduced at a qualitative level (see Fig. 10) it is to be expected that the flow field statistics are well reproduced.

Figures 19a-19c show a zoom-in of the region close to the swirler exit and display contours of the spray diameter, droplet temperature and mean axial velocity respectively thus providing a qualitative representation of the spray dispersion. Regarding droplet dispersion it can be seen in Fig. 19 that the small droplets disperse more rapidly and are thus mostly present at the outer part of the spray cone whilst the large droplets remain in the centre. This is expected from a physical point of view, the higher inertia of the larger droplets leads to higher radial velocities through the forward flow balancing their tangential

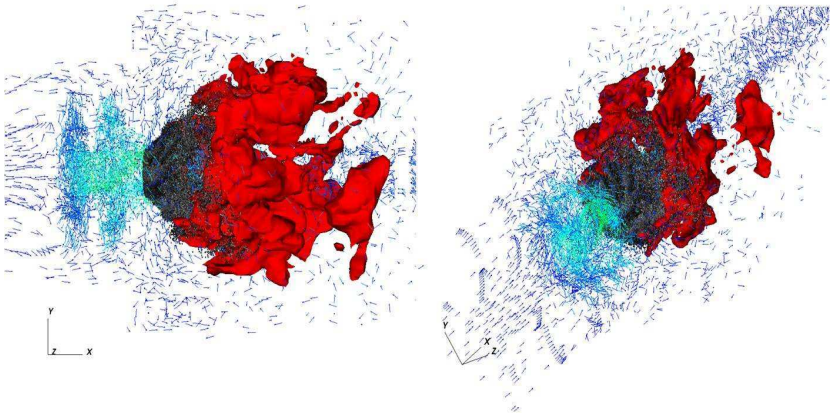

Figure 17: 3-D plot of the instantaneous velocity (arrows), droplet distribution (black dots) and temperature iso-contour for T=2100K

velocity. Also the droplet temperatures are higher at the location where larger droplets are present (at the centre of the branches). These droplets also appear to have higher velocities. It is interesting to note that droplets are still present even at gas temperatures higher than 1500K (the area is indicated by the red line in the figures) which implies a complex flame structure with the coexistence of premixed combustion(air with vapour created from the vaporisation process at $z < 15$mm)that has already occurred and non-premixed combustion from the liquid droplets that are still present at this location. Looking again at Figs. 12, 11 diffusion flame is expected to be located close to the areas with the stoichiometric mixture fraction. However there are pockets of high temperature inside the zone of the stoichiometric mixture fraction that probably correspond to premixed flames. These findings are consistent with a recent work by Luo et al. [57]. The droplets that enter the high temperature zone are the bigger droplets that take longer to evaporate fully.

Figure 20 shows the evolution of the droplet size *pdf* at different axial locations for both the reactive and the equivalent non-reactive cases in order to better understand how combustion alters the rate of evaporation and thus the distribution of the droplets. In both cases the initial *pdf* ($z = 0$) corresponds to a Rosin-Rammler *pdf* with a mean droplet size of $6\mu$m. For the combusting case, Fig. 20(a) it can be seen that initially (for $z < 20$mm) the proportion of large droplets is maintained close to the initial distribution consistent with the smallest droplets disappearing almost at the same rate as the large ones reduce in size. Further downstream, as the droplets enter the reaction zone and their temperatures increases rapidly, the large droplets continue heating up but the temperature of the smaller droplets reaches boiling point at an increased rate. The flattering of the *pdf* indicates that the large droplets reduce in size slower than the rate of disappearance of the small ones. In other words the number of small droplets, initially larger after entering the combustion zone reduces

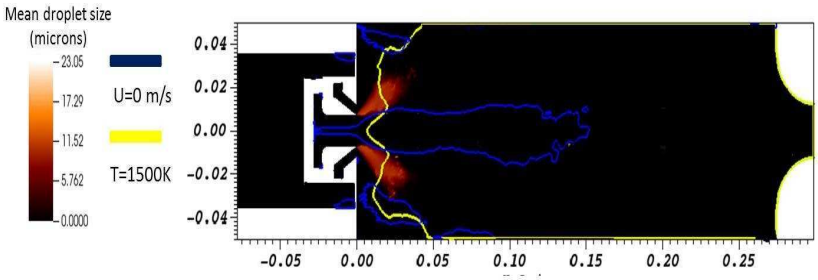


Figure 18: Slice of the velocity field (arrows) and droplet diameter contour. The yellow line indicates the iso-contour of T=1500K and the blue line the iso-contour of zero velocity in order to locate the recirculation zone.

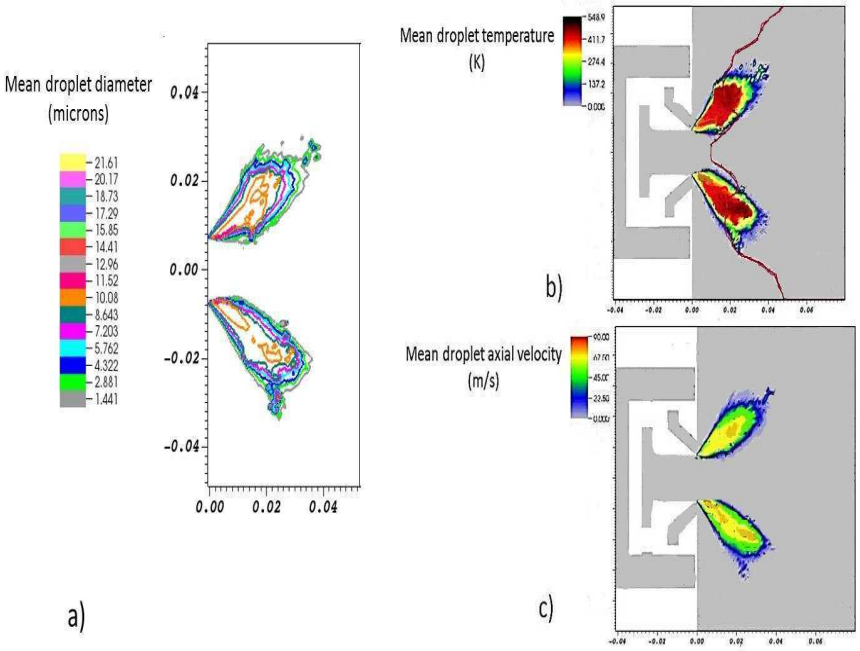


Figure 19: Mean axial velocity field and spray diameter, temperature and axial velocity contours. The red line limits the area with flow temperature higher than 1500K.

rapidly and at some point balances out the number of the large droplets that evaporate slower.

Figure 20(b) shows the evolution of the droplet size *pdf* for a case equivalent to reactive case A in which no ignition process is applied and thus the underlying flow field temperature remains relatively constant. The behaviour of the droplet-size *pdf* is significantly different. Although there is no combustion, the initial temperature of the droplets is 295 K, significantly lower from the temperature of the underlying flow field (550 K) causing the droplets to heat up and evaporate, at a rate different to that of the previous case. The *pdf* starts flattening out almost immediately downstream, indicating that the small droplets disappear quicker than the rate that the large ones reduce in size since the latter do not immediately reach the boiling point. It should be noted here that the comparison of the two cases is only qualitative as the flow fields are different and this influences the dispersion of the droplets (see Fig. 9). This is likely to affect to a certain extent the movement of the droplets closer to the swirler exit where the recirculation is created and thus the behaviour of the droplet-size *pdf*.

Figure 21 shows a comparison of measured and simulated spray *pdfs* at different axial and radial locations. Squares represent the experiments [10, 11], and lines the LES simulations with 8 stochastic fields. The computed *pdfs* were reconstructed from samples collected from the simulations over one flow through time and their lack of smoothness arises because of small finite volumes of the flow solver. Nevertheless it can be seen that the *pdf* is reproduced to a reasonable accuracy by the simulations.

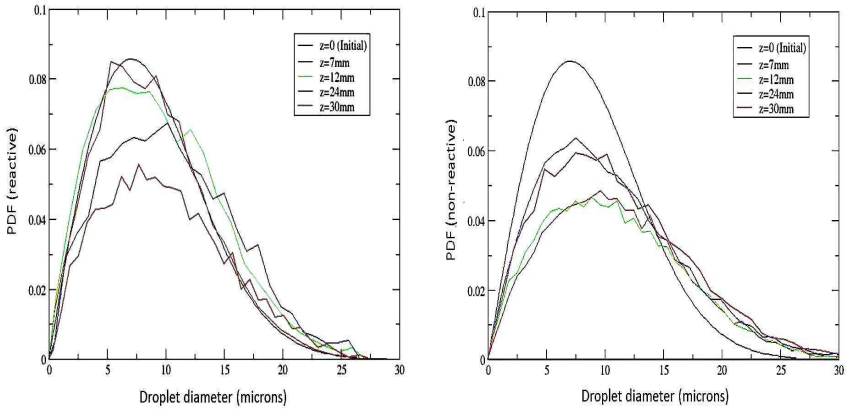


(a) (b)

Figure 20: Spray *pdf* at different axial locations: (a) Reactive case, (b) Non-reactive case

The measured and simulated radial profiles of the three components of droplet velocity are compared in Fig. 22 at three axial locations close to the injector. Squares represent the experiments [10, 11], black lines the simulations

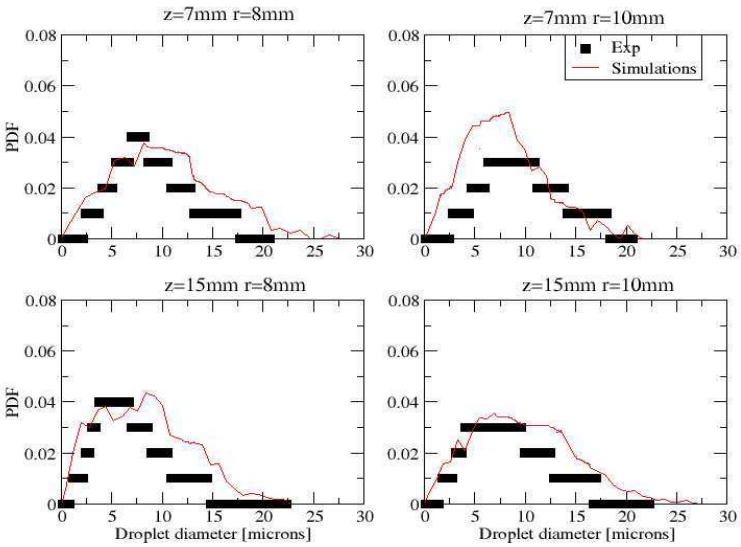


Figure 21: Spray *pdf* at different axial and radial locations. Squares represent the experiments [10, 11], and lines the LES simulations with 8 fields.

with one field and the red lines simulations with eight stochastic fields. To aid the comparison the simulated for gas phase velocities (dashed lines) are also included. The width of the simulated recirculation zone of the gas phase and that of the dispersed phase are similar and both simulations (with one and eight fields) reproduce quite accurately the experimental data. However at the downstream locations the agreement with the measured profiles is improved when eight stochastic fields are used, ie the influence of sgs fluctuations are included. An interpretation of these results is aided when they are viewed together with Fig. 23 in which the radial profiles of the droplets Sauter mean diameters (SMD) at six axial locations are presented. The experimental data shows that only a very small decrease of SMD is observed with increasing downstream distance. Also relatively small radial variations are present, except in the region of the recirculation zone where the size of the droplets reduces considerably. This size distribution is typical of a hollow cone atomiser where the smaller size droplets are entrained in the core and the larger droplets travel to the edge of the spray. As the droplets travel downstream they evaporate and the radial distribution tends to become more uniform. This behaviour is captured reasonably accurately both quantitatively and qualitatively by the simulations. The inclusion of the *sgs* fluctuation model, by increasing the number of fields from one to eight stochastic fields improves the results in the areas around the edges of the recirculation zone ($r = 10$mm). This can be explained by the temperature profiles presented in Fig. 13. The simulated gas phase temperatures at these locations are slightly higher if eight fields are included (see Figs 13 to 14). In

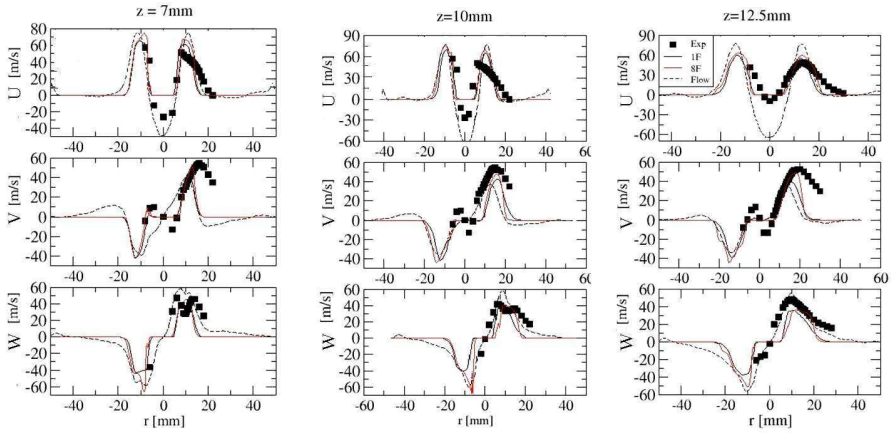


Figure 22: Radial profiles of particle velocities at different axial locations. Squares represent the experiments [10, 11], the dashed lines the LES simulations with 1 field and the solid lines the LES simulations with 8 fields.

terms of mean flow field statistics a difference of an order of 20 K may not be considered significant but an equivalent increase in the droplet temperature (see Fig. 24) will considerably change the droplet size because of its effect on the droplet evaporation rate. This is most pronounced at locations some way downstream of the injector where the droplets have already started to heat up due to the preheated flow field. The higher gas field temperature results also affect the droplet velocity. Since the droplet size is captured more accurately the dispersion, dependent on droplet diameter, is also more accurately reproduced. As expected the smaller droplets follow closer the gas phase flow field streamlines, as can be seen in Figs.22 and 23. In the recirculation zone there is disagreement because according to the simulations no droplets are present in this zone, whereas the measurements indicate the presence of droplets. An explanation for this is difficult to provide. The smaller droplets are expected to follow the gas flow and thus enter the recirculation zone as can be seen from the measured SMDs and corresponding velocities at 7 mm and 10mm. However, if these small droplets acquire a negative velocity and enter the recirculation zone where the temperatures are higher than 1500 K then they are likely to evaporate rapidly. It may be, however, that these discrepancies are related to the high temperatures in the centreline observed in Fig. 13.

In order to investigate in more detail the relationship between the three variables, temperature, velocity and diameter that characterise droplet dispersion and evaporation the results at two locations are considered. The first is close to the swirler exit ($z = 7$mm) and the second is in the fully burning region at $z = 30$mm. At the first location close to the injector where the recirculation zone is developed the sub-grid contribution is important. The second position is more indicative of the performance of the *sgs* combustion model. As the radial profiles of the mean and rms of velocities and temperatures do not show

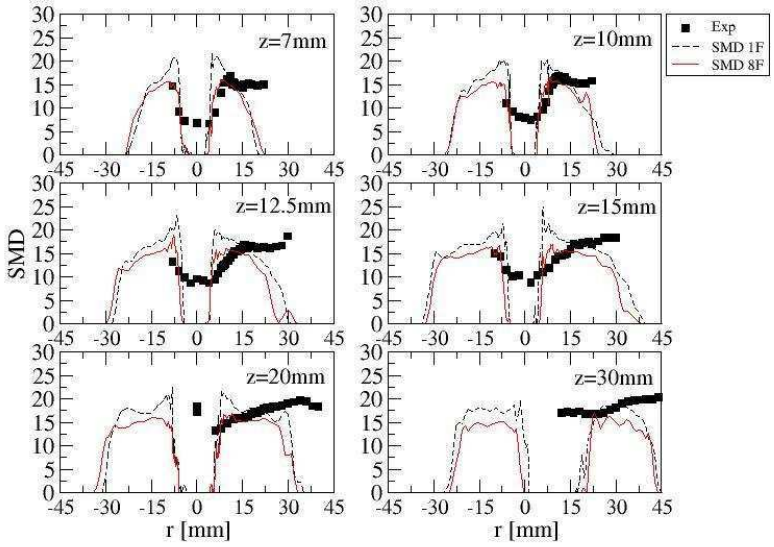


Figure 23: Radial profiles of SMD at different axial locations. Squares represent the experiments [10, 11], the dashed lines the LES simulations with 1 field and the solid lines the LES simulations with 8 fields.

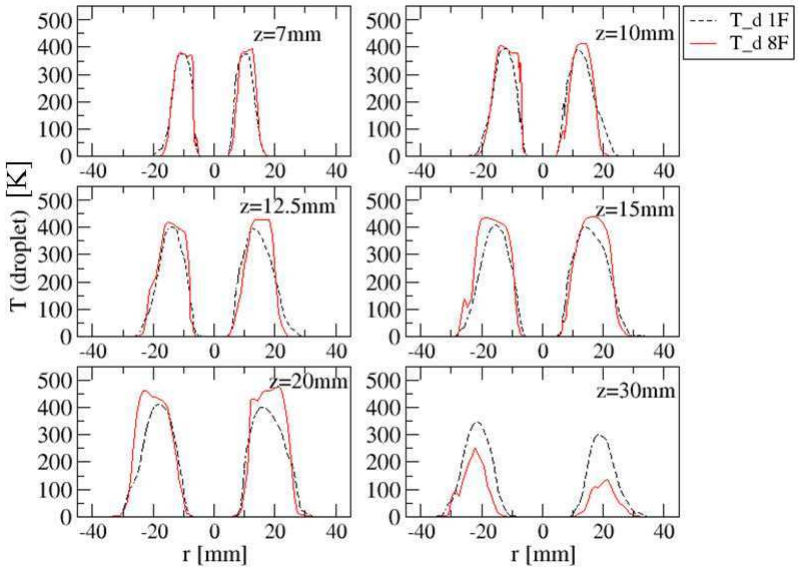


Figure 24: Radial profiles of the droplets' temperature at different axial locations. Dashed lines represent the LES simulations with 1 field and solid lines the LES simulations with 8 fields.

any significant differences a more detailed examination of droplet statistics is provided.

Figures 25(a) and 25(b) show scatter plots of mean droplet velocity against droplet diameter at a downstream location of $z = 7$mm and $z = 30$mm for one and eight stochastic fields, ie with and without the *sgs* combustion model; pseudo-colour represents mean droplet temperature. The two results show very little difference at the first location, as expected because there is no combustion in this region. However there appears to be clear correlation between diameter and velocity suggesting that the random term of Eq. (7) does not play a significant role, especially for the smaller diameters, in this region. In the case of the second location the differences between the one and eight field solutions are larger with the droplet diameters and velocities being essentially uncorrelated with the *sgs* combustion model. An interesting branching phenomenon is also evident at the top left figure which implies that droplets with the same diameter have different axial velocities depending their temperature.

## 6. Conclusions

In the present work LES is applied to the simulation of the two-phase flow in the GENRIG combustor, which is an aeronautical-type swirl stabilised spray burner, fuelled by Jet-A liquid kerosene. An Eulerian description of the continuous phase is adopted and is fully coupled with a Lagrangian description of the dispersed phase. Comparisons of the LES results with measurements for the non-reacting case demonstrate that the essential features of the flow are reproduced to a good level of accuracy. In the combusting case the results indicate that the simulated flame structure is similar with and without the inclusion of the *sgs* combustion model. However the simulated spray statistics differ considerably with the two cases and the results serve to demonstrate the importance of the *sgs* combustion model. The model for the dispersed phase - the fuel spray - used in this study reproduces the SMD and the velocity of the droplets very accurately. Some discrepancies between the experimental data and simulations are evident in the recirculation zone and these are mostly attributable to the uncertainty in the inlet spray boundary conditions and thus further experimental investigation is desirable. A second issue that needs to be investigated in future work is the suitability of a Lagrangian formulation for the dispersed phase close to the injector. The method used is mostly valid for a dilute spray with droplet sizes sufficiently small so that they can be considered as point sources of mass, momentum, species and energy. However, in areas close to the injection point the liquid phase is not always present in the form of droplets but rather as liquid blobs or ligaments of size comparable to the scales of the motion of the continuous phase.

## Acknowledgements

This work received funding from the European Community through the project TIMECOP-AE (Project No. AST5-CT-2006-030828). It reflects only

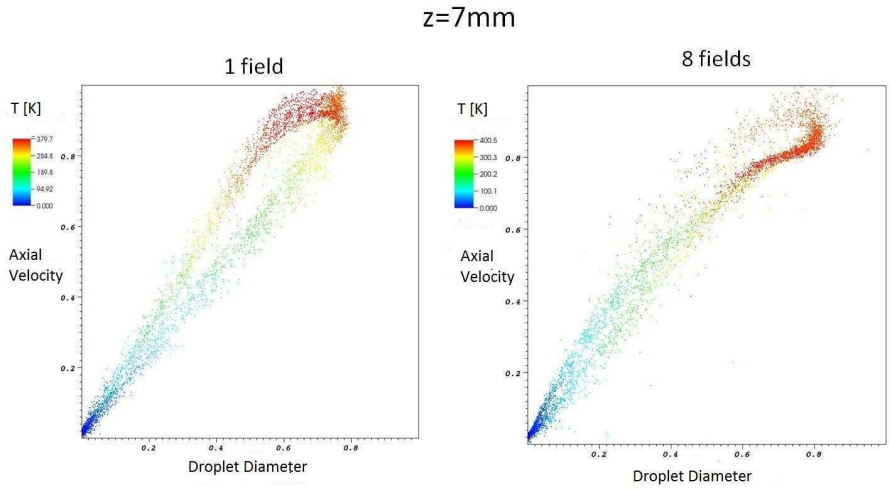


(a)

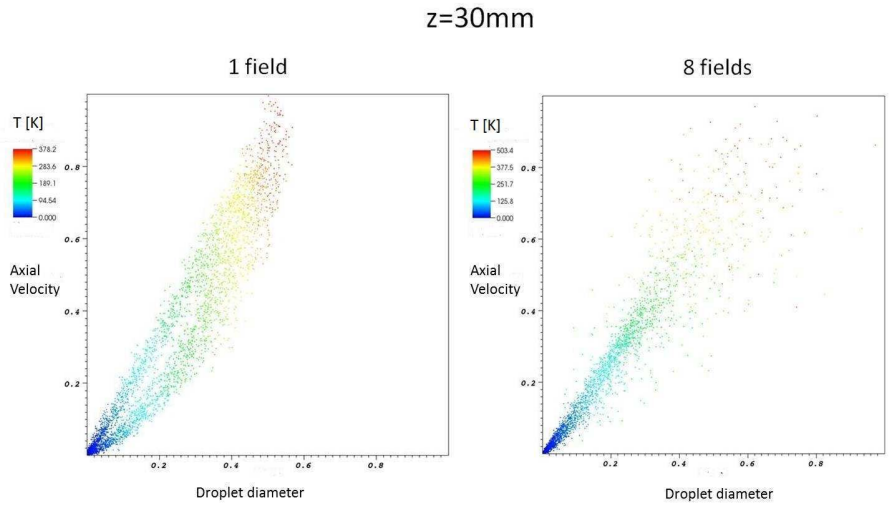


(b)

Figure 25: Scatter plots of mean droplet velocity against diameter at *(a)* $z = 7$mm and at *(b)* $z = 30$mm for one and eight fields. Pseudo-colour represents mean droplet temperature

the authors' views and the Community is not liable for any use that may be made of the information contained therein. The authors are also grateful to Dr C. Goddard for providing the grid used in the present calculations and Dr S. Navarro-Martinez for valuable discussions.

## References

## References

[1] K. Mahesh, G. Constantinescu, S. Apte, G. Iaccarino, F. Ham, P. Moin, Large-eddy simulation of reacting turbulent flows in complex geometries, Journal of Applied Mechanics 73 (3) (2006) 374–381.

[2] G. Boudier, L. Y. M. Gicquel, T. J. Poinsot, D. Bissières, C. Bérat, Comparison of LES, RANS and experiments in an aeronautical gas turbine combustion chamber, Proceedings of the Combustion Institute 31 (2) (2007) 3075–3082.

[3] G. Boudier, L. Y. M. Gicquel, T. J. Poinsot, Effects of mesh resolution on large eddy simulation of reacting flows in complex geometry combustors, Combustion and Flame 155 (1-2) (2008) 196 – 214.

[4] M. Boileau, S. Pascaud, E. Riber, B. Cuenot, L. Gicquel, T. Poinsot, M. Cazalens, Investigation of two-fluid methods for large eddy simulation of spray combustion in gas turbines, Flow, Turbulence and Combustion 80 (2008) 291–321.

[5] Ying-wen Yan, Jian-xing Zhao, Jing-zhou Zhang, Yong Liu, Large-eddy simulation of two-phase spray combustion for gas turbine combustors, Applied Thermal Engineering 28 (1112) (2008) 1365 – 1374.

[6] T. Lederlin, H. Pitsch, Large-eddy simulation of an evaporating and reacting spray, Tech. rep., Center for Turbulence Research, Annual Research Briefs (2008).

[7] S. V. Apte, K. Mahesh, P. Moin, Large-eddy simulation of evaporating spray in a coaxial combustor, Proceedings of the Combustion Institute 32 II (2009) 2247 – 2256.

[8] M. Sanjose, J. Senoner, F. Jaegle, B. Cuenot, S. Moreau, T. Poinsot, Fuel injection model for Euler-Euler and Euler-Lagrange Large-Eddy Simulations of an evaporating spray inside an aeronautical combustor, Int. J. Multiph. Flow 37 (2011) 514–529.

[9] G. Hannebique, P. Sierra, E. Riber, B. Cuenot, Large eddy simulation of reactive two-phase flow in an aeronautical multipoint burner, Flow, Turbulence and Combustion 90 (2013) 449–469.

[10] U. Meier, J. Heinze, S. Freitag, C. Hassa, Spray and flame structure of a generic injector at aeroengine conditions, in: Proceedings of ASME Turbo Expo 2011: Power for Land, Sea and Air: GT2011, Vol. GT2011-45282, Vancouver, Canada, 2011.

[11] S. Freitag, U. Meier, J. Heinze, T. Behrendt, C. Hassa, Measurement of initial conditions of a kerosene spray from a generic aeroengine injector at elevated pressure, Proc. 23rd Annual Conference on Liquid Atomization and Spray Systems, (ILASS-Europe 2010), Brno, Czech Republic ISBN-978-80-7399-997-1 (137).

[12] C. Goddard, S. Sadig, S. Stow, M. Zedda, Toward innovative methods for combustion prediction in aero-engines, Tech. rep., EU Project TIMECOP-AE D4.1.8.

[13] S. Elghobashi, On predicting particle-laden turbulent flows, Applied Scientific Research 52 (4) (1994) 309 – 29.

[14] J. Smagorinsky, General circulation experiments with the primitive equations, Journal of Monthly Weather Review 91 (1963) 99–164.

[15] U. Piomelli, J. Liu, Large-eddy simulation of rotating channel flows using a localized dynamic model, Physics of Fluids 7 (4) (1995) 839 – 48.

[16] S. B. Pope, PDF methods for turbulent reactive flows, Prog. Energy Combust. Sci. 11 (2) (1985) 119–192.

[17] M. Bini, W. P. Jones, Large-eddy simulation of particle-laden turbulent flows, Journal of Fluid Mechanics 614 (207-252).

[18] M. Bini, W. P. Jones, Large eddy simulation of an evaporating acetone spray, International Journal of Heat and Fluid Flow 30 (3) (2009) 471 – 480.

[19] C. Gardiner, Handbook of Stochastic Methods, Springer-Verlag, New York, 1984.

[20] M. Bini, W. P. Jones, Particle acceleration in turbulent flows: A class of nonlinear stochastic models for intermittency., Phys. Fluids 19 (2007) 035104.

[21] M. Yuen, L. W. Chen, On drag of evaporating droplets, Comb. Sci and Tech. 14 (1976) 147–154.

[22] W. Sirignano, Fuel droplet vaporization and spray combustion theory, Prog. Energy Combust. Sci 9 (4) (1983) 291–322.

[23] G. M. Faeth, Evaporation and combustion of sprays., Progress in Energy and Combustion Science 9 (1-2) (1983) 1 – 76.

[24] V. Sankaran, S. Menon, Les of spray combustion in swirling flows, Journal of Turbulence 3 (2002) N11.

[25] W. Ranz, W. Marshall, Evaporation from drops: Part I, Chem. Eng. Prog. 48 (3) (1952) 141–146.

[26] W. Ranz, W. Marshall, Evaporation from drops: Part II, Chem. Eng. Prog. 48 (3) (1952) 173–180.

[27] E. M. Sparrow, J. L. Gregg, The variable fluidproperty problem in free convection, Trans Am. Soc. Mech. Engrs 80 (1958) 879–886.

[28] G. L. Hubbard, V. F. Denny, A. Mills, Droplet evaporation: effects of transients and variable properties, Int. J. Heat Mass Transfer 18 (1975) 1003–1008.

[29] G. M. FAETH, R. S. LAZAR, Fuel droplet burning rates in a combustion gas environment, AIAA Journal 9 (11) (1971) 2165–217.

[30] J. Pozorski, S. V. Apte, Filtered particle tracking in isotropic turbulence and stochastic modeling of subgrid-scale dispersion, International Journal of Multiphase Flow 35 (2) (2009) 118 – 128.

[31] W. P. Jones, S. Lyra, A. J. Marquis, Large Eddy Simulation of a droplet laden turbulent mixing layer, Int. J. Heat Fluid Flow 31 (2010) 93–100.

[32] W. P. Jones, S. Lyra, A. J. Marquis, Large Eddy Simulation of Evaporating Kerosene and Acetone Sprays, Int. J. Heat Mass Trans. 53 (2010) 2491–2505.

[33] W. P. Jones, S. Lyra, S. Navarro-Martinez, Large Eddy Simulation of a swirl stabilized spray flame, Proc. Comb. Inst. 33 (2011) 2153–2160.

[34] W. P. Jones, S. Lyra, S. Navarro-Martinez, Large Eddy Simulation of Swirling Kerosene Spray Flames, Comb. Flame 159 (2011) 1539–1561.

[35] E. E. O'Brien, The probability density function (pdf) approach to reacting turbulent flows, in: P. Libby, F. Williams (Eds.), Turbulent Reacting Flows, Springer-Verlag, 1980, pp. 185–218, appeared under 'Topics in Applied Physics', vol.44.

[36] W. Kollmann, Pdf transport equations for chemically reacting flows, in: R. Borghi, S. Murthy (Eds.), Turbulent Reactive Flows, Spinger-Verlag, 1989, pp. 715–730.

[37] F. Gao, E. E. O'Brien, A large eddy simulation scheme for turbulent reacting flows, Physics of Fluids A 5 (1993) 1282–1284.

[38] C. Dopazo, E. E. O'Brien, Functional formulation of nonisothermal turbulent reactive flows, Phys. Fluids 17 (1968).

[39] J. Villermaux, L. Falk, A generalized mixing model for initial contacting of reactive fluids, Chem. Eng. Sci. 49 (24B) (1994) 5127–5140.

[40] W. P. Jones, S. Navarro-Martinez, Large eddy simulation of autoignition with a subgrid probability density function method, Combustion and Flame 150 (3) (2007) 170–187.

[41] W. P. Jones, V. N. Prasad, Large eddy simulation of the sandia flame series (d-f) using the eulerian stochastic field method, Combustion and Flame 157 (9) (2010) 1621–1636.

[42] C. Dopazo, Probability density function approach for a turbulen axisymmetric heated jet. centerline evolution, Phys. Fluids 18 (1975) 397–404.

[43] L. Valiño", A field monte carlo formulation for calculating the probability density function of a single scalar in a turbulent flow, Flow, Turbulence and Combustion 60 (1998) 157–172.

[44] V. Sabel'nikov, O. Soulard, Rapidly decorrelating velocity-field model as a tool for solving one-point fokker-planck equations for probability density functions of turbulent reactive scalars, Physical Review E (Statistical, Nonlinear, and Soft Matter Physics) 72 (1) (2005) 16301–1.

[45] A. Garmory, R. E. Britter, M. E., Simulation of the evolution of aircraft exhaust plumes including detailed chemistry and segregation, Journal of geophysical research 113 (8) (2008) D08303–D08303.

[46] A. Garmory, E. Mastorakos, Aerosol nucleation and growth in a turbulent jet using the stochastic fields method, Chemical Engineering Science 63 (16) (2008) 4078–4089.

[47] W. P. Jones, R. P. Lindstedt, Global reaction schemes for hydrocarbon combustion, Combustion and Flame 73 (3) (1988) 233–249.

[48] W. P. Jones, A. Tyliszczak, Large eddy simulation of spark ignition in a gas turbine combustor, Flow, Turbulence and Combustion 85 (3-4) (2010) 711–734.

[49] J. Luche, Elaboration of reduced kinetic models of combustion: application to a kerosene mechanism, Ph.D. thesis, LCSR Orléans (2003).

[50] B. Franzelli, E. Riber, M. Sanjose, T. Poinsot, A two-step chemical scheme for kerosene-air premixed flames, Combust. Flame 157 (2010) 1364–1373.

[51] W. P. Jones, F. di Mare, A. J. Marquis, LES-BOFFIN: Users Guide, Technical Memorandum, Imperial College, London (2002).

[52] B. J. Van Leer, Towards the ultimate conservative difference scheme: II Monotonicity and conservation combined in a second order scheme, Comp. Phys. 14 (1974) 361–370.

[53] U. Piomelli, E. Balaras, Wall layer models for large eddy simulation, Annual Review of Fluid Mechanics 34 (2002) 349–374.

[54] P. E. Kloeden, E. Platen, Numerical solution of stochastic differential equations, Springer-Verlag, New York, 1992.

[55] M. Rachner, Die stoffeigenschaften von kerosin jet a-1, Tech. rep., Institut fur Antriebstechnik, DLR, Koln (1998).

[56] I. A. Dodoulas, S. Navarro-Martinez, Large eddy simulation of premixed turbulent flames using the probability density function approach, Flow, Turbulence and Combustion 90 (2013) 645–678. doi:10.1007/s10494-013-9446-z.

[57] K. Luo, H. Pitsch, M. Pai, O. Desjardins, Direct numerical simulations and analysis of three-dimensional n-heptane spray flames in a model swirl combustor, Proceedings of the Combustion Institute 33 (2) (2011) 2143–2152.

**List of Figures**